Powder Technology 220 (2012) 104–121

Contents lists available at SciVerse ScienceDirect

Powder Technology

journal homepage: www.elsevier.com/locate/powtec

Numerical analysis of the dynamics of two- and three-dimensional fluidized bed reactors using an Euler–Lagrange approach

Perrine Pepiot [a], Olivier Desjardins [b,*]

[a] National Bioenergy Center, National Renewable Energy Laboratory, Golden, CO, United States
[b] Department of Mechanical Engineering, University of Colorado at Boulder, Boulder, CO, United States

ARTICLE INFO

Available online 19 September 2011

Keywords:
Fluidized bed
Euler–Lagrange
Three-dimensional simulation
Large-scale simulation
Bubble dynamics
Residence time

ABSTRACT

Biomass thermochemical conversion, often done in fluidized beds, recently gained a lot of attention due to its potential to efficiently produce renewable liquid fuels. Optimization of reactor design and operating conditions, however, requires a fundamental understanding of bed dynamics. In this work, a numerical framework based on an Euler–Lagrange approach is developed and used to perform and analyze large-scale simulations of two- and three-dimensional periodic fluidized beds. Collisions are handled using a soft-sphere model. An efficient parallel implementation allows one to explicitly track over 30 million particles, which is representative of the number of particles found in lab-scale reactor, therefore demonstrating the capability of Lagrangian approaches to simulate realistic systems at that scale. An on-the-fly bubble identification and tracking algorithm is used to characterize bubble dynamics for inlet velocities up to 9 times the minimum fluidization velocity. Statistics for gas volume fraction, gas and particle velocities, bed expansion, and bubble size and velocity, is compared across the two- and three-dimensional configurations, and comparison with literature data generally shows good agreement. The wide distribution of gas residence times observed in the simulations is linked to the different gas hold-up characteristics of the gas–solid system.

1. Introduction

Biomass thermochemical conversion processes such as gasification and pyrolysis hold great promise for the production of second and third generation biofuels and will play a determining role in meeting the U.S. renewable fuels targets set for the next 20 years. However, current technologies face significant challenges, noticeably increasing the risks associated with the development of industrial-scale facilities. In gasification for example, a major contribution to the overall process cost comes from the necessary clean-up and conditioning step before the syngas can be used for liquid fuel synthesis [1]. To ensure that biomass-derived fuels become cost-competitive in the short term, optimization of reactor design and operating conditions, based on a fundamental understanding of the dense gas–solid reactive mixture, is essential and has to take advantage of the remarkable progress in multiphase computational fluid dynamics (CFD).

Fluidization is a process of choice for biomass conversion [2], and therefore, will be the focus of the present work. There are two main approaches to simulate the dense particulate flows encountered in fluidized bed reactors. Utilizing the analogy with a fluid, Eulerian methods are built on the assumption that the solid and gas phases are two inter-penetrating media. Computationally affordable, and therefore well-suited for large-scale reactor simulations, they however require the introduction of numerous assumptions and models to describe the evolution of the solid phase and its coupling with the surrounding gas phase. Most derivations of the governing equations use the kinetic theory of granular flows [3] to formulate closure models for unclosed terms, which can become challenging, especially when dealing with evolving polydisperse systems [4]. An alternative and very promising approach solves for the moments of the joint probability density function of particle position and velocity using, for example, closures based on a quadrature strategy (quadrature method of moments (QMOM) [5,6]).

On the other hand, the Lagrangian particle tracking (LPT) approach, also called discrete particle method (DPM), represents the disperse phase by considering each particle independently and solving for their trajectories. The explicit consideration of the individual particles allows for a convenient implementation of detailed models of their chemical and physical evolution, but at a relatively high computational cost, which restricts its range of application. A major contribution to the overall cost of this approach comes from the representation of collisions between particles. Several techniques have been developed to handle collisions, the most commonly used being the event-driven hard-sphere model [7,8], and the soft-sphere model based on the analogy between two particles colliding and a spring-dashpot-slider system [9,10]. An alternative approach, the multiphase particle-in-cell (MP-PIC) method, solves for the particle distribution function by tracking parcels of particles, and assumes

* Corresponding author.
E-mail address: olivier.desjardins@cornell.edu (O. Desjardins).

0032-5910/$ – see front matter
doi:10.1016/j.powtec.2011.09.021

that the collision forces are proportional to the gradient of a function of the particle volume fraction [11,12]. More details can be found in the review by Deen et al. [13]. Lagrangian techniques have been applied to numerous problems, including sedimentation [14], bubble formation [15,16], or segregation in a binary system [17–19]. Also, they provide a natural framework to develop and investigate the validity of Eulerian modeling assumptions, such as particle velocity distribution, particle pressure, or granular temperature [20,21].

Validation of the numerical results, while essential for model development, proves to be especially challenging, since flow visualization and measurements are noticeably difficult to perform in fluidized beds. A review of existing experimental techniques to measure gas–solid distribution in fluidized beds can be found in Van Ommen and Mudde [22]. These techniques include direct visualization of two-dimensional or dilute systems, tomography (electric capacitance or nuclear) to obtain voidage distribution of a cross-section of the bed, optical and capacitance probes, and pressure and acoustic measurements using pressure taps.

Most measurements have been done in pseudo-2D beds using digital imaging techniques. A non-exhaustive list includes the work of Goldschmidt et al. [23,24] for mono- and bi-disperse systems, providing experimental segregation rate, and instantaneous and time-averaged particle distributions at inlet velocities up to twice the minimum fluidization velocity. The latter results were qualitatively compared to a discrete particle and a two-fluid simulation. The observed differences between both numerical approaches were attributed to the lack of particle rotation in the two-fluid model. Hoomans et al. [25] obtained particle velocity maps, occupancy plots and speed histograms from Positron Emission Particle tracking in a bed fluidized at 1.5 times the minimum fluidization velocity, and highlighted the importance of the collision parameters in LPT simulations to correctly reproduce experimental data. Particle Image Velocimetry, coupled with digital image analysis, was used to obtain time-averaged particle flux map and segregation rate in a bi-disperse two-dimensional bed by Deen et al. [17], and results were compared with a LPT simulation. Busciglio et al. [26,27] used a digital image analysis technique to extract quantitative information on bed expansion, and bubble hold-up, size evolution, distribution, density, aspect ratio, and rising velocity from a series of fluidization experiments in a pseudo-two dimensional reactor in which the inlet velocity was varied from 1.7 to 7 times the minimum fluidization velocity U_{mf}. Experimental data were appropriately reproduced by an Eulerian–Eulerian two-dimensional simulation of the reactor.

Detailed measurements other than pressure fluctuations in three-dimensional reactors are much scarcer. Among these, Kawaguchi et al. [28] measured the particle velocity distribution in a cylindrical spouted bed using nuclear magnetic resonance imaging (NMR Imaging or MRI), and compared it to a hybrid 2D (for the flow)–3D (for the particle motion) LPT simulation. Van der Lee et al. [29] used X-ray fluoroscopy to determine the average bubble diameter in a cylindrical reactor. They showed that the experimental results agreed well with the correlation by Werther et al. [30]. Heindel et al. [31] used digital X-ray radiography and stereography imaging to visualize and time-resolve 3D flow structures in multiphase and opaque fluid flows. The technique has been used to investigate gas holdup in a cylindrical fluidized bed reactor containing two different materials, glass beads and ground walnut shells [32], and in a reactor with a side jet [33,34]. Time-averaged gas volume fractions and bed height were compared to two- and three-dimensional Eulerian simulations [32,34]. Both numerical works included a grid refinement study, and looked at the impact of the drag model on gas hold-up.

Since most measurements are available only in pseudo-two dimensional reactors, with a third direction usually several particle diameter wide, two main questions arise, namely the capability of 2D models to represent the pseudo-2D experiments, and the appropriateness of 2D or pseudo-2D configurations to study flow dynamics of fully 3D reactors. Using a two-fluid model to simulate a pseudo-2D reactor, Peirano et al. [35] reported a significant difference in bed height between 2D and 3D results, the 2D bed height being much larger. They linked the discrepancy to differences in maximum packing. A more comprehensive study was conducted by Xie et al. [36], again using an Eulerian approach. Cylindrical and box reactors were both considered, and in contrast to the work cited above, the third direction was wide enough for structures to fully develop. Differences between two and three dimensions increased significantly as the inlet velocity was increased. Again, the 2D Eulerian model was shown to over-predict bed height and gas velocities. A budget analysis [37] highlighted the role of non-axial terms in the observed differences, these terms becoming more important at higher velocities.

In the present work, a Lagrangian particle tracking approach is used to investigate the dynamics of fluidized bed reactors. The reduced number of necessary assumptions, the ease of implementation of particle models and the potential for LPT simulations to provide a convenient framework for Eulerian model development and testing motivated this choice. The numerical methods employed to solve the gas phase governing equations are tailored for turbulence, and therefore applicable to the complex three-dimensional flows expected during high velocity fluidization. The numerical tool's very good conservation properties, efficient parallel structure, and advanced use of Message Passing Interface provide the ideal setting to demonstrate the feasibility of large-scale simulations of fluidized bed reactors using LPT. A fundamental approach is followed, focusing on periodic configurations to extract the intrinsic dynamics of fluidized beds. Two and three-dimensional cases with different fluidization velocities are considered, allowing for a detailed comparison of the bed statistics. A bubble identification and tracking algorithm provides quantitative information on bubble number, size, and velocity. The mathematical description of the problem will be given first, followed by the numerical methodology employed. The configurations and simulation parameters will then be provided. Finally, results will be presented and discussed.

2. Mathematical description

The gas phase is modeled as a Newtonian fluid assumed to follow the low Mach number Navier–Stokes equations, while the dispersed phase is treated as a collection of individual particles that move according to Newton's second law. In this work, the fluidized beds are considered non-reactive in order to focus on cold flow dynamics. The two phases are strongly coupled through momentum exchange at the surface of each particle. Since some regions in a fluidized bed reactor may be near the close-packing limit, particle collisions are critical to predicting bed dynamics and are therefore taken into account. The gas phase equations are first discussed, followed by the particle equations. Then, the coupling terms between gas and solid phases are described. Finally, the collision model is presented.

2.1. Gas phase description

The detailed description of the gas–particle system involves the classical Navier–Stokes equations for the gas phase, Newton's laws of motion for the particles, and no-slip, no-penetration boundary conditions at the surface of each particle. This approach would require that the flow around each particle be resolved, which is prohibitively expensive for the scales of interest here. In order to account for the effect of the particles in a tractable manner, a point-particle assumption is introduced, allowing the gas phase equations to be filtered. Several strategies can be used for that purpose. In particular, Anderson and Jackson [38] derive a set of equations using local volume averaging. In their work, the averaging volume is chosen such that it is significantly larger than the particle volume, while ideally remaining smaller than the smallest macro/mesoscopic phenomena of interest. Another strategy based on ensemble averaging is proposed by

Zhang and Prosperetti [39], which leads to very similar equations. Regardless of the strategy followed, the locally averaged gas phase evolution equation takes the form of a variable density, low Mach number Navier–Stokes equation, modified to take into account the effective volume occupied by the particulate phase, with the addition of a volumetric source term to account for momentum exchange with the particles, as well as unclosed stresses due to the averaging operation. Several approaches have been proposed for handling these unclosed terms, such as combining them with the stress tensor [38], accounting for them through the introduction of an effective viscosity [39,14], or simply neglecting them altogether [40]. In this work, these additional unclosed stresses are neglected. Consequently, unless specified otherwise, all variables can be considered to be locally volume-averaged quantities over a characteristic volume V, chosen to be at least an order of magnitude larger than the particle volume V_p.

Conservation of mass is written

$$\frac{\partial}{\partial t}\left(\varepsilon_f \rho_f\right) + \nabla\cdot\left(\varepsilon_f \rho_f u_f\right) = 0, \tag{1}$$

where u_f is the fluid velocity, ρ_f is the fluid density, ε_f is the local volume fraction of fluid, and t is time. Similarly, conservation of momentum is written as

$$\frac{\partial}{\partial t}\left(\varepsilon_f \rho_f u_f\right) + \nabla\cdot\left(\varepsilon_f \rho_f u_f u_f\right) = \nabla\cdot\tau + \varepsilon_f \rho_f g - F^{\text{inter}}, \tag{2}$$

where g is the gravitational acceleration, F^{inter} is the interphase momentum transfer term between the particles and the fluid, which is described in Section 2.3, and τ is the stress tensor. The stress tensor is defined by

$$\tau = -p\mathbb{I} + \sigma, \tag{3}$$

where p is the hydrodynamic pressure and σ is the viscous stress tensor, defined by

$$\sigma = \mu\left(\nabla u_f + \nabla u_f^T\right) - \frac{2}{3}\mu\nabla\cdot u_f\ \mathbb{I}, \tag{4}$$

with μ the dynamic viscosity.

2.2. Solid phase description

The position of individual particles evolves according to

$$\frac{dx_p}{dt} = u_p, \tag{5}$$

where x_p is the position of a particle and u_p is its velocity, which, according to Newton's second law of motion, obeys

$$m_p \frac{du_p}{dt} = f^{\text{inter}} + F^{\text{col}} + m_p g. \tag{6}$$

In the previous equation, m_p is the mass of the particle, defined by $m_p = \pi\rho_p d_p^3/6$ where ρ_p is the particle density and d_p is the particle diameter. F^{col} is the particle collision force, which is described in Section 2.4. f^{inter} is the momentum exchange term for a single particle, related to F^{inter} through

$$F^{\text{inter}} = \frac{1}{V}\sum_{i=1}^{n_p} f_i^{\text{inter}}, \tag{7}$$

where n_p is the number of particles in the volume V.

2.3. Interphase exchanges

The force f^{inter} that couples the particle and the gas phase comes from the momentum exchange at the particle surface due to the boundary conditions, namely

$$f^{\text{inter}} = \int_{\partial V_p} \tau'\cdot n dS. \tag{8}$$

In the previous relation, τ' is the pointwise (i.e. non-averaged) fluid stress tensor, and n is the normal vector to the particle surface ∂V_p. Since the fluid variables have gone through an averaging procedure, τ' is not readily available, and modeling assumptions need to be introduced. A typical strategy is to write $\tau' = \tau + \tau''$, where τ'' is the difference between the pointwise and the averaged stress tensor. Assuming that this difference is due to the presence of the particle, the surface integral of τ'' corresponds then to the drag force, i.e.

$$f^{\text{inter}} = \int_{\partial V_p} \tau\cdot n dS + f^{\text{drag}}. \tag{9}$$

The locally averaged fluid stress tensor does not vary significantly on the scale of the particles, hence one can write

$$f^{\text{inter}} = \int_{V_p} \nabla\cdot\tau dV + f^{\text{drag}} \approx V_p \nabla\cdot\tau + f^{\text{drag}}. \tag{10}$$

As pointed out by Kafui et al. [41], this formulation is in agreement with the classical two-fluid model equations, and is equivalent to writing $f^{\text{inter}} = f^{drag}$ while multiplying the stress tensor by ε_f in Eq. 2.

The drag force on a particle f^{drag} normalized by the drag force on a single, isolated sphere in a Stokes flow, is assumed to be a function of the local gas volume fraction and particle Reynolds number Re_p only. Accordingly,

$$\frac{f^{\text{drag}}}{m_p} = \frac{18\mu\varepsilon_f}{\rho_p d_p^2}\left(u_f - u_p\right) F\left(\varepsilon_f, \text{Re}_p\right). \tag{11}$$

The dimensionless drag force coefficient F is taken from the work by Beetstra et al. [42], who developed a correlation valid for a wide range of Reynolds numbers and particle volume fractions,

$$F\left(\varepsilon_f, \text{Re}_p\right) = 10\frac{1-\varepsilon_f}{\varepsilon_f^2} + \varepsilon_f^2\left(1 + 1.5\sqrt{1-\varepsilon_f}\right) + \frac{0.413\text{Re}_p}{24\varepsilon_f^2}\left(\frac{\varepsilon_f^{-1} + 3\varepsilon_f\left(1-\varepsilon_f\right) + 8.4\text{Re}_p^{-0.343}}{1 + 10^{3\left(1-\varepsilon_f\right)}\text{Re}_p^{-0.5-2\left(1-\varepsilon_f\right)}}\right), \tag{12}$$

where the particle Reynolds number is defined by

$$\text{Re}_p = \frac{\rho_f d_p \left|u_f - u_p\right|}{\mu}. \tag{13}$$

2.4. Collision model

As mentioned above, several approaches can be used to describe collisions, including volumetric, hard, and soft-sphere models. In this work, the soft-sphere model, illustrated by Fig. 1, is chosen for scalability and accuracy reasons.

When two particles are close to each other or slightly overlapping, a repulsive force is created, whose magnitude depends on the distance between the two particles, their relative velocity, a spring stiffness, and a damping parameter. Such a model dynamically prevents particles from overlapping when approaching the maximum packing limit. Accordingly, the repulsive force on a particle a due to a collision with a particle b can be written

$$f_{b\to a}^{\text{col}} = \begin{cases} (k\delta - \eta(u_a - u_b)\cdot n)n & \text{if } d_{ab} < (r_a + r_b + \lambda), \\ 0 & \text{else.} \end{cases} \tag{14}$$

In this expression, $r_{a/b}$ is the radius of particle a/b, d_{ab} is the distance between the centers of the particles a and b, δ is the overlap between

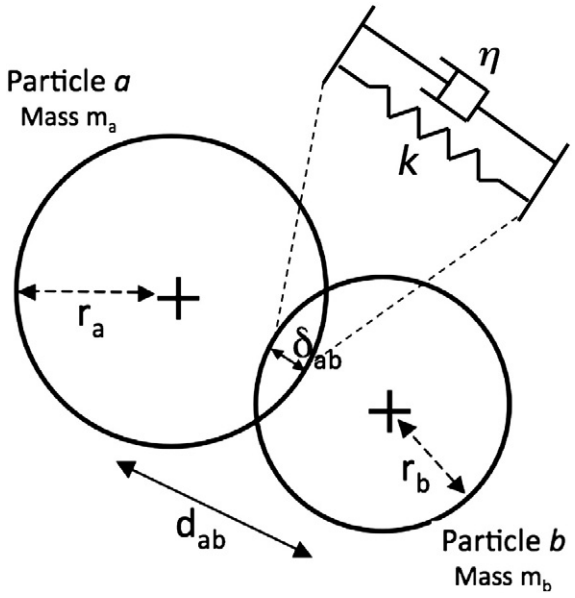

Fig. 1. Soft-sphere representation of a particle–particle collision using a spring-dashpot model.

the particles, $u_{a/b}$ is the velocity of particle a/b, and n is the unit vector from the center of particle b to that of particle a, as illustrated in Fig. 1. λ is the force range, a small number set to create a collision force when two particles are close together, but not strictly overlapping yet, adding some numerical robustness to the collision scheme. k is the spring stiffness, η is the damping parameter, expressed as

$$\eta = -2\ln e\frac{\sqrt{m_{ab}k}}{\sqrt{\pi^2+(\ln e)^2}},\quad \text{with}\quad m_{ab}=\left(\frac{1}{m_a}+\frac{1}{m_b}\right)^{-1}. \tag{15}$$

In the above equations, $0<e<1$ is the restitution coefficient, and $m_{a/b}$ is the mass of particle a/b. By symmetry, $f^{\text{col}}_{a\to b}=-f^{\text{col}}_{b\to a}$. Collisions on the walls of the reactor are handled by treating the walls as particles with infinite mass and zero radius. The full collision force that each particle feels can then be expressed as

$$F_i^{\text{col}} = \sum_{\substack{\text{particle } j\\ \text{colliding with } i}} f^{\text{col}}_{j\to i}. \tag{16}$$

Note that a similar approach can be used in order to handle inter-particle friction [10], although it requires time-integrating the tangential displacement and keeping track of the angular momentum of particles. Because of the added computational cost, it was decided not to include tangential inter-particle motion. Since we are interested in ideal rigid spheres, such an assumption is not expected to affect the validity of our results significantly, especially at higher inlet gas velocities. It might however affect the relevance of our two-dimensional results at lower inlet velocities.

3. Numerical methodology

3.1. Flow and particle solver

The equations presented above are implemented in the in-house flow solver NGA [43], an arbitrarily high order multi-physics CFD code for large eddy and direct numerical simulations. This code has been used in numerous studies for combustion-related applications, including liquid atomization [44–47], spray dynamics, spray combustion [48], premixed, partially-premixed, and non-premixed turbulent jets [49,50] and combustion in technical devices, such as large-scale furnaces [51], internal combustion engines, and aircraft engine afterburners. NGA solves the low-Mach number Navier–Stokes equations using a fully conservative finite difference scheme of arbitrarily high accuracy. For all simulations presented below, the computations are performed using second order accuracy in space. Time advancement is accomplished using the second order accurate semi-implicit Crank–Nicolson scheme of Pierce and Moin [52]. Based on a fractional step approach [53], this algorithm uses both temporal and spatial staggering between velocity and volume fraction, as illustrated in Fig. 2. The details on the mass, momentum, and energy conservative finite difference scheme are available in [43].

Because we rely on a pressure projection step to ensure mass conservation, an efficient and robust Poisson solver is key to ensuring the performance of the NGA code. Here, the black-box multigrid (BBMG) solver of Dendy [54] is used. The implementation of the BBMG follows the three-dimensional description introduced in Dendy [54]. The relaxation step consists of an 8-color Gauss–Seidel, which is most natural to parallelize with 27-point stencils in three dimensions. The finest grid level is partitioned using the same domain decomposition strategy as in NGA, and the domain decomposition of coarser grid levels simply follows from the finest decomposition. Finally, the BBMG was introduced as a preconditioner to a conjugate gradient solver. The full solver is ideally suited for solving the Poisson equation efficiently on parallel architectures.

The particle equations consist of a set of six coupled ordinary differential equations per particle, which are solved using a second-order Runge–Kutta scheme. The particles are distributed among processors based on the underlying domain decomposition of the gas phase domain. After each time-step, they undergo an inter-processor communication step as they move from one processor sub-domain to another. The computation of the collision force requires measuring inter-particle distances, which leads to an $O(N_p^2)$ problem if implemented using a brute-force strategy. Instead, NGA makes use of the underlying computational mesh in order to speed up the identification of likely collision partners: for each particle p, we identify the computational cell i_p, j_p, k_p that it belongs to. For this cell and its closest 26 neighbors, we then loop over all particles p' in that cell, and test whether p and p' are colliding. The computational cells are large enough to ensure all collisions are captured using this approach. Note that NGA also relies on ghost particles in order to facilitate the parallel implementation of the collision force. These ghost particles correspond to particles located inside ghost cells, and they are communicated between processors like any Eulerian variable.

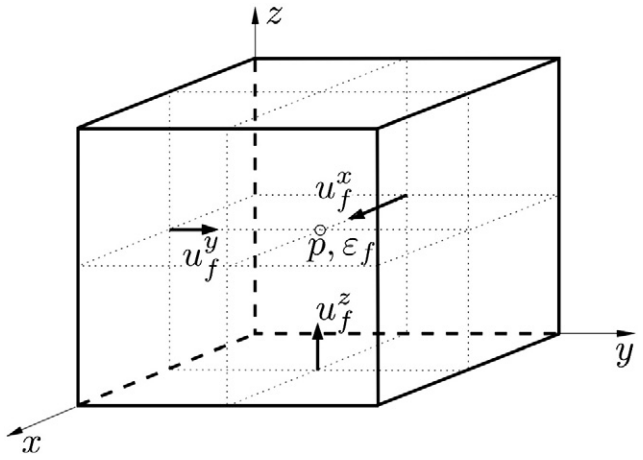

Fig. 2. Staggered variable arrangement in NGA.

3.2. Two-way coupling

The solid particles and the gas phase are explicitly coupled through the F^{inter} term in Eqs. 2, 6, and 7, and through the volume fraction in Eqs. 1 and 2. In addition, the particle drag is affected by the local gas velocity and stress tensor.

Particles are updated before each new flow solver time-step, outside of the Crank–Nicolson subiterations. Consequently, the temporal accuracy of the coupling between particles and gas phase is limited to first order. However, temporal errors are unlikely to be significant, considering the small time-step size typically used in order to resolve particle collisions. The choice of time-step size is detailed in Section 3.3.

To interpolate the gas phase values to a particle position, a second order trilinear interpolation scheme is used, based on the convolution of linear interpolations in each spatial direction. The mapping of particle properties to the Euler mesh, needed for example in Eq. 7, is usually done using trilinear extrapolation as well [12,14]. However, if the ratio of particle diameter over mesh size is too large, this extrapolation method can produce significant oscillations in the extrapolated data, leading to numerical instabilities. In addition, standard trilinear extrapolation is not a conservative operation. Instead, a more accurate method is employed here, that relies on a mollification approach to smoothly and conservatively extrapolate the particle force onto the gas phase mesh. The particle force is transferred onto the flow solver mesh using a mollification kernel ζ with characteristic size δ, as shown in Fig. 3(a) ζ is a vanishing function defined by

$$\begin{cases} \zeta(s) = \frac{1}{4}s^4 - \frac{5}{8}s^2 + \frac{115}{192} & \text{if} \quad s \le 0.5 \\ \zeta(s) = -\frac{1}{6}s^4 + \frac{5}{6}s^3 - \frac{5}{4}s^2 + \frac{5}{24}s + \frac{55}{96} & \text{if} \quad s \le 1.5 \\ \zeta(s) = \frac{(2.5-s)^4}{24} & \text{if} \quad s \le 2.5 \\ \zeta(s) = 0 & \text{else}, \end{cases} \tag{17}$$

where $s = |x|/\delta$ is the scaled distance from the particle center (see Fig. 3(a)). The characteristic length δ is taken as the gas phase mesh size Δx. Consequently, the particle force is typically spread out over the 27 nearest cells surrounding the particle. The extrapolated force at each grid node i, $\tilde{f}_i^{\text{inter}}$ is obtained from the particle force using

$$\tilde{f}_i^{\text{inter}} = \gamma_i f^{\text{inter}} \tag{18}$$

with

$$\gamma_i = \frac{\int_{V_i} \zeta(s)ds}{\sum_{\text{all cells } j} \int_{V_j} \zeta(s)ds}, \tag{19}$$

where V_i is the volume of cell i, and the sum in the denominator is conducted over all cells inside the support of the mollification kernel. The normalization ensures that the particle force is conserved when transferred to the gas phase (i.e. $\sum \gamma_i = 1$ for each particle). An accurate implementation of the mollification approach depends on the accuracy of the numerical computation of the integrals in Eq. 19. Here, a numerical integration scheme based on Gauss quadrature is used, providing spectral accuracy for the evaluation of the integral. This technique efficiently provides a high order, fully conservative strategy for transferring particle data back to the underlying Eulerian mesh. This approach is employed both for creating the interphase exchange term F^{inter} and the gas volume fraction ε_f. More details can be found in Desjardins and Pepiot [55].

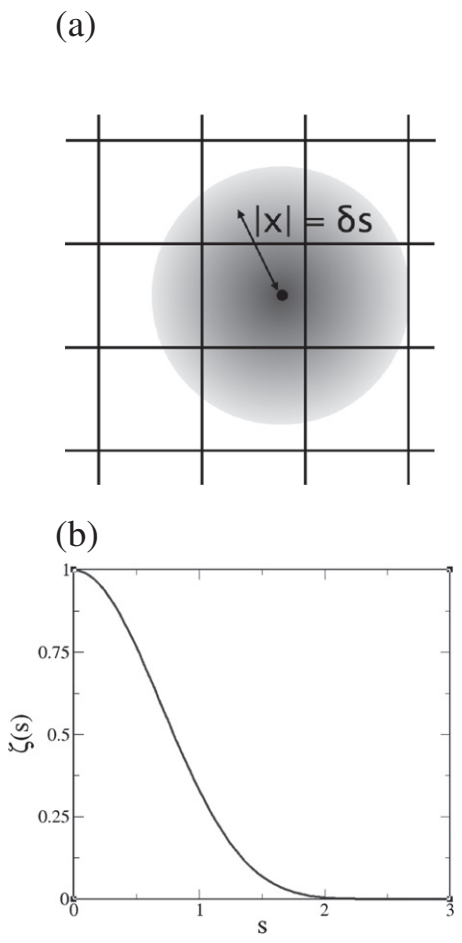

Fig. 3. Extrapolation of a particle quantity onto the gas phase mesh. (a) Distribution of the particle data onto the surrounding cells based on a distance function. (b) Mollification kernel ζ.

3.3. Resolution criteria

The gas phase equation is written for locally volume-averaged quantities, where the characteristic averaging volume V has to be at least an order of magnitude larger than the volume of a particle V_p, say $V \sim 10V_p$. Therefore, the smallest possible structure that can be expected to arise in the gas phase will be limited to a characteristic volume of about $10V_p$. Consequently, the gas phase equations should be fully resolved spatially if the mesh size Δx is chosen such that $\Delta x \sim (10\pi/6)^{1/3} d_p \sim 1.74 d_p$. This represents the finest mesh size for the point particle approach described above to remain valid.

Out of all the Courant–Friedrichs–Lewy (CFL) conditions, the most stringent constraint is given by particle interactions, which are controlled both by a particle-specific CFL, as well as by the characteristic collision timescale. First, a particle CFL number can be defined by

$$\text{CFL}_p = \frac{\Delta t_p |u_p|}{d_p}, \tag{20}$$

where Δt_p is the particle time-step size. It characterizes what fraction of its diameter a particle moves in a time step. In order to limit the inter-particle overlap, it is necessary to keep this number small, and 0.1 is the upper limit that we will use in all the simulations. Then, the particle integration time step is also limited by the characteristic collision timescale,

$$\tau_{\text{col}} = 2\sqrt{\frac{m_{ab}}{k}}. \tag{21}$$

However, a realistic value of k would lead to a computationally intractable problem. Instead, $\Delta t_p \leq \tau_{col/5}$ is used to define k, while Δt_p is chosen by considering $CFL_p \leq 0.1$. This ensures that the inter-particle overlap is limited to at most a few percent of the diameter, while ensuring that collisions are fully resolved.

4. Configuration and simulation parameters

The fluidization of solid spherical particles in simple configurations is considered in this work. The particle density and diameter match the synthetic olivine sand currently used at the National Renewable Energy Laboratory (NREL) in a new 4 in. fluidized bed reactor designed to study biomass gasification and pyrolysis [56]. Gas properties are those of nitrogen at room temperature. The corresponding physical parameters are given in Table 1.

Both two- and three-dimensional configurations are being investigated, whose general layout is given in Fig. 4. Arrays of particles in a simple cubic arrangement with a particle volume fraction of 0.4 initially fill the bottom part of the computational domain, up to an initial bed height $H_0 = 0.075$ m. In the absence of a better macro-scale reference length, we will make use of H_0 for non-dimensionalization purposes. A uniform velocity profile is imposed at the bottom, and a convective outflow condition is imposed at the exit. Periodic boundary conditions are imposed on the sides of the domain so that wall effects on bed dynamics are eliminated and only the intrinsic bubbling behavior is captured. Particles collide with the top and bottom boundaries, which prevents them from exiting the domain, and thus keeps the number of particles in the bed constant.

The grid spacing is about 1.86 times the particle diameter, in accordance to Section 3.3. Thanks to the mollification strategy described above, the particle–gas coupling remains robust. The computational domain has to be wide enough for the structures to freely evolve and grow across the bed. To find the minimum domain width that satisfies this requirement, a series of increasingly wide two-dimensional domains is considered, and statistics are collected from fluidization simulations conducted at constant inlet velocity. The simulation parameters are displayed in Table 2 (cases P_1 to P_5), while the corresponding statistics for mean gas volume fraction, gas velocity, and fluctuations of gas volume fraction are shown in Fig. 5. While the two narrowest cases P_1 and P_2 lead to significant deviation from the reference case P_5, no significant differences in the statistics are observed for the P_3 and P_4 intermediate domain widths. However, accounting for the increased computational cost of considering a larger domain, it was observed that converged statistics were obtained slightly faster in the P_4 case than for P_3 configuration. Therefore, the domain width for two-dimensional configurations is set to the P_4 value, while the lower domain width of the P_3 case is chosen for three-dimensional simulations. Gas inlet velocities were selected to cover several regimes, from light bubbling to turbulent fluidization. Following experimental practice, the inlet velocity U_{in} is expressed as a factor of the minimum fluidization velocity U_{mf} of the system [3],

$$U_{mf} = \frac{d_p^2 \Delta\rho g}{150\mu_f} \frac{\varepsilon_{mf}^3}{1-\varepsilon_{mf}}. \quad (22)$$

In Eq. 22, ε_{mf} is the porosity at minimum fluidization, assumed to be $\varepsilon_{mf} = 1-\pi/6 = 0.476$ for spheres in a cubic arrangement [3]. Due to the relatively high computational cost of three-dimensional simulations, a single inlet velocity of five times the minimum fluidization velocity was selected. Parameters for all the simulations conducted in this work are shown in Table 2 (cases R_1 to R_5) for the 2D cases, and in Table 3 for the 3D case. Note that the length of the R_4 and R_5 reactors, associated with higher inlet velocities, has been increased to accommodate higher average bed heights.

Table 1
Gas and particle physical characteristics.

Parameter	Units	Value
Gas density ρ_f	[kg.m^{-3}]	1.13
Gas viscosity μ	[kg.m^{-1}.s^{-1}]	1.77e−5
Particle density ρ_p	[kg.m^{-3}]	3300
Particle diameter d_p	[m]	2.1e−4
Gravity g	[m.s^{-2}]	9.81

The simulations were conducted on Red Mesa, which is a new NREL high performance computing system located at the Sandia National Laboratories in Albuquerque, NM. Red Mesa is devoted exclusively to research and development for renewable energy applications. The system consists of 1920 2.93 Ghz dual-socket quad core, Nehalem x5570 processor nodes, for a total of 15,360 cores with a peak performance of 180 TFlops. The scaling properties of the NGA code on this system were found to be excellent, with more than 85% scale-up efficiency with 382 million particles on up to 4096 cores. The bubbling process being highly unsteady in nature, statistical convergence of the results requires extended computational time. This is especially true in 2D cases: converged statistics on average required 25 flow-through times, corresponding to a cost for each two-dimensional cases of about 25,000 core hours. The more expensive three-dimensional configuration allows for faster statistical convergence, which was considered satisfactory in about 8 flow-through times. The total cost for this simulation was close to 250,000 core hours, or 5 days on 2000 cores. For all cases, statistics are gathered after the initial transient has been replaced with a statistically stationary bubbling process.

5. Results and discussion

5.1. Visualization

While fluidization processes are notoriously difficult to visualize experimentally, time and space-resolved simulations offer unrestricted access to the inside of the reactor, and visualization of tangible variables such as particle location or bubbling activity is an excellent way to first qualitatively assess the validity of the numerical models.

Fig. 6 shows sequential snapshots of the particles location for the two-dimensional simulation series *R1* to *R5*, in 50 ms time increments.

Below four times the minimum fluidization velocity, the bed shows very little activity, with small bubbles forming mostly near the top of the bed. When increasing the inlet velocity, more bubbles can be observed, appearing closer to the bottom of the bed and growing to larger sizes. The total instantaneous volume occupied by bubbles increases significantly with the inlet velocity, considerably raising the average bed height. At $U_{in} = 9\ U_{mf}$, it becomes difficult to identify separate bubble entities, as very large void regions directly connect to the gas-filled upper part of the reactor. Bubble bursting events are well defined at low inlet velocities, with small pockets of particles being ejected from the bed. However, at higher velocities, the interface between bed and free-board becomes more blurry, and particles are carried higher in the reactor. While a comparatively more intense bubbling activity has been reported at low inlet velocities [25], the qualitative behavior of the bed when the inlet velocity is increased is in agreement with experimental observations [27,57].

Fig. 7 shows results from the three-dimensional simulation. An iso-surface of high gas volume fraction, $\varepsilon_f = 0.85$, is used to visualize the envelope of bubbles forming inside the reactor. Colored panels show the gas velocity magnitude.

In agreement with the corresponding two-dimensional simulation *R3*, bubbles are formed mostly near the bottom of the bed with an initial tubular shape, and further expand into mushroom-like shapes as they rise toward the top of the bed. At any given level in the reactor, both large and small bubbles co-exist, the smallest ones either disappearing on their own or merging with larger bubbles. Gas velocities are strongly correlated with the presence of bubbles, but also display large-scale patterns in the higher part of the bed, likely associated

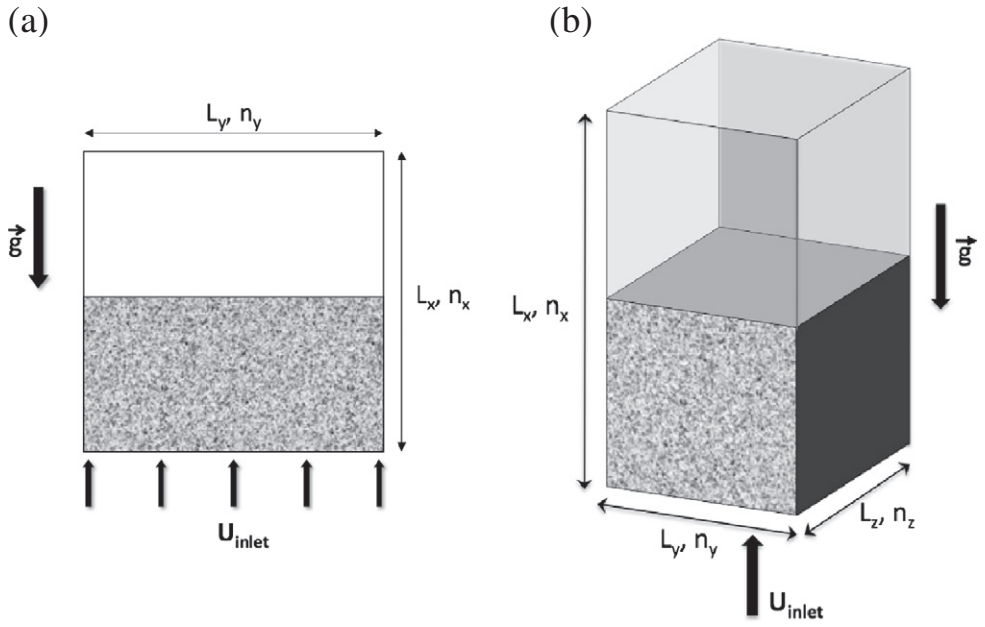

Fig. 4. Schematics of the computational domains used in the numerical simulations. (a) Two dimensional. (b) Three-dimensional.

with bursting events. Bubbles are smoothly expanding and moving up the bed, much like in a liquid–gas system.

While overall, the dynamics of the bed as perceived through visualization of the particle positions are qualitatively in agreement with experimental observations, a more quantitative approach is required to gain confidence in the accuracy of the numerical models used in the simulations.

5.2. Bed statistics

Cross-section and time-averaged evolution of the main variables such as gas volume fraction and gas velocities as a function of the height in the reactor have been collected until no significant changes in the statistics were observed. This required around 25 flow-through times, defined as L_x/U_{in}, for each 2D simulation, and about 8 flow-through times for the 3D case. Fig. 8 shows the resulting statistics for the two-dimensional cases *R1* to *R5*, where the streamwise coordinate has been non-dimensionalized by the initial bed height H_0. Note that the total reactor height for the low velocity cases *R1* and *R2* was equal to $2H_0$, while it was increased to $4H_0$ for the high velocity cases *R3* to *R5*.

As the inlet velocity increases, Fig. 8(a) shows that the profile of mean gas volume fraction changes drastically, from a step function at 3.75 U_{mf} to a quasi-linear increase at the highest velocity simulated.

Table 2
Parameters used in the two-dimensional fluidized bed reactor simulations.

Name	Reactor dimension ($L_x \times L_y$, [m])	Grid size	n_p	U_{in}
P_1	0.15×0.05	384×48	53,138	5 U_{mf}
P_2	0.15×0.0625	384×96	79,544	5 U_{mf}
P_3	0.15×0.075	384×192	106,276	5 U_{mf}
P_4	0.15×0.15	384×384	212,552	5 U_{mf}
P_5	0.15×0.3	384×768	425,430	5 U_{mf}
R_1	0.15×0.15	384×384	212,552	3.75 U_{mf}
R_2	0.15×0.15	384×384	212,552	4 U_{mf}
R_3 (=P_4)	0.15×0.15	384×384	212,552	5 U_{mf}
R_4	0.3×0.15	768×384	212,552	7 U_{mf}
R_5	0.3×0.15	768×384	212,552	9 U_{mf}

Average packing in the bed, defined as one minus the mean gas volume fraction $<\varepsilon>$, decreases from a value close to the nominal packing at minimum fluidization ($\varepsilon_{mf}=0.476$) to around 0.25, which is consistent with the observed bed expansion at higher inlet velocities. Bed height, while easily defined at low fluidization velocity, is more difficult to appraise at higher velocities. For comparison purposes, bed height is defined here as the streamwise location in the reactor below which 99% of the particles are found, and is shown in Fig. 9. In addition, error bars show the maximum and the minimum bed heights over the length of the simulations. Bed height mean and fluctuations increase with the fluidization velocity, which is in good agreement with previous studies [27]. The bed height appears to be slightly larger than that reported by Busciglio et al. [27], which could be due to the lack of inter-particle friction in our mathematical model, although the case studied here is noticeably different from theirs.

The mean streamwise gas velocity, shown in Fig. 8(b), exhibits a high and nearly constant value in the bed at low inlet velocities, and a linear decrease with streamwise location at higher velocities. In all cases, the mean gas velocity relaxes toward the expected superficial velocity, albeit at different heights. Fig. 8(b) also shows the average value of $\varepsilon_f u_f$, which remains exactly constant through the reactor, thereby confirming that mass is conserved. Particle axial velocity, shown in Fig. 8(c), is statistically close to zero, as can be expected for stationary bubbling fluidized beds.

Fig. 8(d), (e) and (f) display the gas volume fraction, gas streamwise, and cross-streamwise velocity variances as function of the position in the reactor. While at low inlet velocities, fluctuations are mostly confined to the vicinity of the top of the bed, where bubble bursting occurs, large fluctuations can be found throughout the bed at higher velocities, which is consistent with the observation that bubbling activity intensifies and extends to the full bed at higher inlet velocities. Note that while volume fraction fluctuations decrease to zero above the bed as expected, fluctuations in gas velocity decrease to a non-zero value, indicating that the gas phase above the bed is turbulent.

Another quantity of interest is the correlation between gas volume fraction and velocity fluctuations, as shown in Fig. 8(g) and (h) for gas and particle, respectively. A positive value indicates that a locally larger gas volume fraction is associated with a locally higher streamwise velocity. This is the case almost throughout all the beds, except

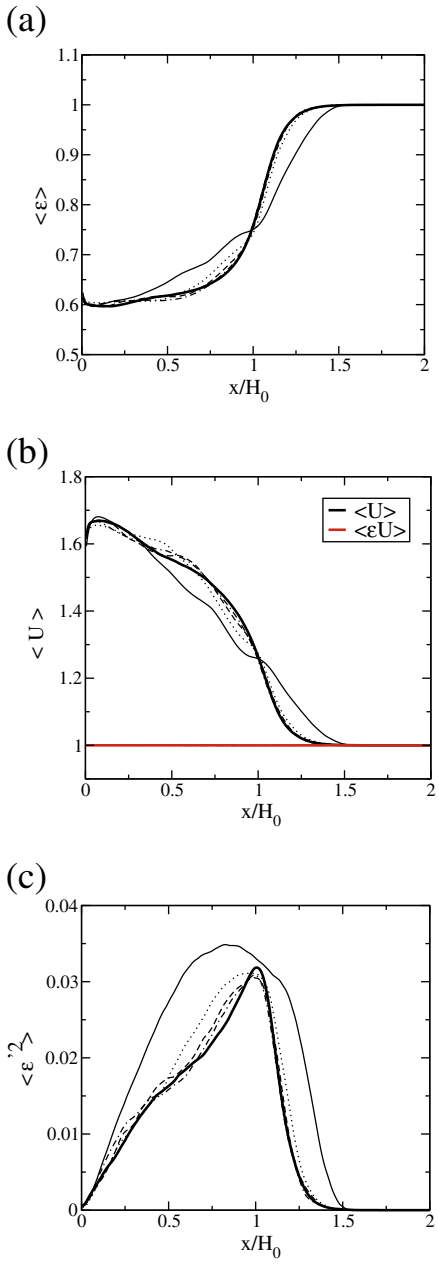

Fig. 5. Mean gas volume fraction, gas velocity and fluctuations of gas volume fraction as a function of height in the reactor for different domain widths (P_1: thin solid line, P_2: dotted line, P_3: dashed line, P_4: dash-dotted line, P_5:thick solid line).

at the very top of the slower beds, suggesting as expected that expanding pockets of gas have a tendency to accelerate upward (bubble rising). The correlation between particle velocity fluctuations and gas volume fraction is more complex, with a tendency to be positive inside the bed, and negative around the bed surface. This suggests that some particles tend to rise inside bubbles inside the bed, leading to a positive correlation. The negative correlation at the bed surface corresponds to bubble bursting events, where the gas volume fraction is higher and particles tend to fall back down toward the bed. Particle velocity fluctuations, shown in Fig. 8(i) for the streamwise and Fig. 8(j) for the cross-streamwise velocity, increase with height in the reactor. Statistics are extremely difficult to converge in the upper part of the reactor due to the small number of particles ejected from the bed, which explains the large oscillations observed in the graphs pertaining to solid particle motion. Finally, dilute regions tend to move faster than denser regions, as shown by the axial gas velocity conditioned on the local gas volume fraction in Fig. 8(k) and (l), with the velocity ratio between dilute and dense regions significantly decreasing as the inlet velocity increases.

To appraise the differences between two- and three-dimensional beds, a comparison of the statistical results for an inlet velocity of 5 U_{mf} was carried out, and is shown in Fig. 10.

Some differences can be observed. First, the bed height is about 10% lower and tends to vary less over time in the three-dimensional case than in two-dimension, as is shown in Fig. 9. This is most likely caused by the difference in maximum packing, since for example, face-centered cubic arrangements in 3D leads to a 74% maximum packing, while it is limited to about 57% in 2D configurations. This fact has been observed before [35,25], and in particular Van Wachem et al. [58] proposed several strategies in order to reconcile 2D Lagrangian simulations with experimental results. However, none of the modifications they proposed recovered all experimental results successfully. It can also be observed that the magnitude of velocity fluctuations is larger, and the ratio between the streamwise velocity in dilute regions and that of denser parts is higher in 3D. This difference may become important when looking at quantities relevant for the chemical processes, such as gas residence time inside the reactor. Note that as expected, 3D statistics in both cross-streamwise directions are similar (e.g. in Fig. 10(f) and (j)). Overall, first order statistics show good agreement between 2D and 3D. However, second order statistics tend to show more noticeable departure. This is in agreement with the prior work of Xie et al. [36,37], who reported increased differences between 2D and 3D at higher fluidization velocities, which are associated with larger velocity fluctuations.

5.3. Gas residence time

Molecular growth leading to tars during biomass gasification is a relatively slow process that will be enhanced by increased gas residence time inside the hot reactor [59,60]. Statistical analysis has shown significant variation of gas velocity depending on the local porosity ε_f (Fig. 8). The simulations presented here can be used to better quantify the variability in residence time of the gas phase. For this purpose, tracer fluid particles were emitted in a continuous fashion at the bottom of the bed and transported by the gas phase. The time needed to reach the mean bed height H was recorded for each of these tracers, allowing one to obtain a residence time distribution for all two- and three-dimensional cases. Results are shown in Fig. 11 for the 2D cases *R1* to *R5*.

In this graph, the x-axis has been normalized by the bulk residence time $t_{\text{bulk}} = H/U_{in}$. At low inlet velocities, a very narrow probability density function (PDF) is obtained, centered around the bulk residence time. However, as the inlet velocity increases, the PDF widens considerably on both sides, with some pockets of gasses requiring more than three times longer or less than a third of the time to exit the bed compared to the bulk flow.

A comparison of the PDF of residence time between 2D and 3D at $U_{in} = 5\ U_{mf}$ is shown in Fig. 12.

Two situations are considered: filled symbols refer to the residence time inside the bed (up to $x = H$), while open symbols refer to the time needed to reach the top of the reactor ($x = L_x = 2H_0$). In the former case, the longest residence times are similar, while the minimum residence times recorded are somewhat smaller in 3D. However, if the time spent in the free-board is taken into account, significantly higher residence times are obtained in 2D compared to 3D. This may be

Table 3
Parameters used in the three-dimensional fluidized bed reactor simulation.

Name	Reactor dimension ($L_x \times L_y \times L_z$, [m])	Grid size	n_p	U_{in}
3D	$0.15 \times 0.075 \times 0.075$	$384 \times 192 \times 192$	34,645,976	5 U_{mf}

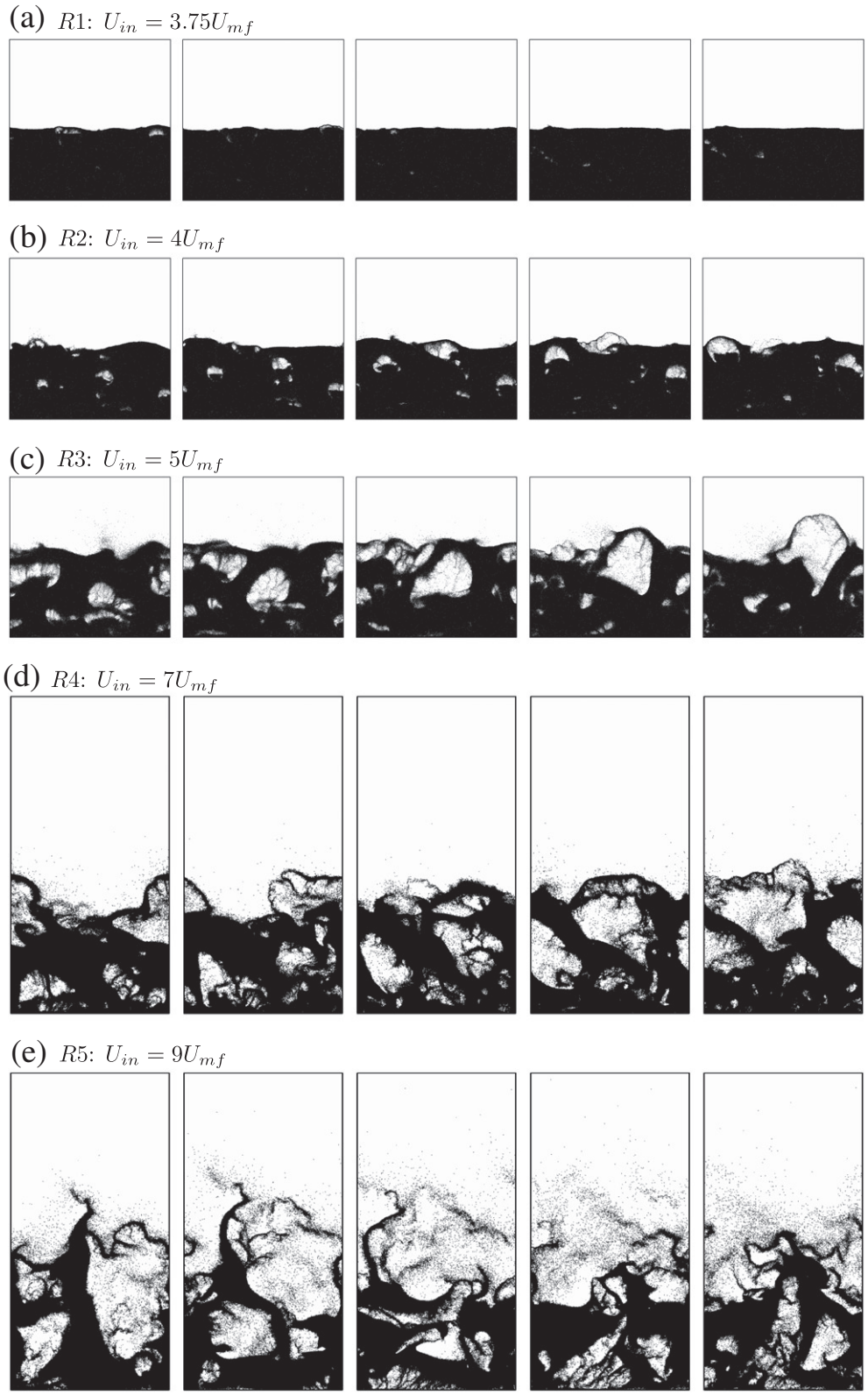

Fig. 6. Particle positions in the 2D periodic fluidized beds *R1* to *R5*. (a) *R1*: $U_{in} = 3.75\ U_{mf.}$ (b) *R2*: $U_{in} = 4\ U_{mf.}$ (c) *R3*: $U_{in} = 5\ U_{mf.}$ (d) *R4*: $U_{in} = 7\ U_{mf.}$ (e) *R5*: $U_{in} = 9\ U_{mf.}$

explained by the turbulent flow observed above the bed, since the dynamics of turbulent flows are inherently 3D, or potentially by differences in the bubble bursting process at the surface of the bed.

To find an explanation to the increased variance observed in Fig. 11, the gas volume fraction encountered by the tracer particles used to evaluate residence times inside the bed (up to $x = H$) were recorded and averaged over the trajectory of the tracers, leading to a path-averaged gas volume fraction ε_t:

$$\langle \varepsilon \rangle_t = \frac{1}{t_{\text{res}}} \int_0^{t_{\text{res}}} \varepsilon(\mathbf{x}_{\text{tracer}}(t))dt. \tag{23}$$

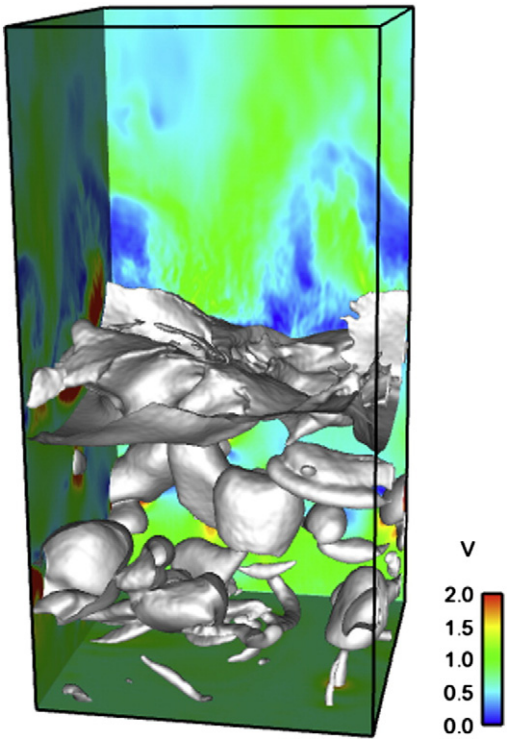

Fig. 7. Visualization of fluidization in a three-dimensional periodic fluidized bed with an inlet velocity $U_{in} = 5U_{mf}$: iso-surface of gas volume fraction $\varepsilon_f = 0.85$ and gas velocity magnitude.

The ensemble-averaged residence times $\{t_{res}\}$ conditioned on ε_t and normalized by the bulk residence time are plotted in Fig. 13 for all cases considered in this work.

The x-axis is rescaled with the average gas volume fraction in the bed ε_{bulk}. Several important observations can be made. First, the range of ε_t increases significantly as the inlet velocity increases, meaning that the gas entering the reactor will encounter a much wider range of conditions at high velocities. This was already visible in Fig. 8(a). Then, gas trapped in bubbles (corresponding to a high ε_t) will reach the top of the bed much faster than gas going through denser parts of the bed (corresponding to low ε_t). The residence time appears to depend almost linearly on ε_t. Finally, when ε_t is normalized by ε_{bulk}, as is done in Fig. 13, all curves seem to collapse on a single profile, with a larger deviation observed for the lowest inlet velocities. Hence, residence time for all cases investigated here appears to be a similar function of the departure between the encountered gas volume fraction and ε_{bulk}. This result suggests a similar mechanism for bubble dynamics, with bubbles allowing for a rapid crossing of the bed and denser regions trapping gas inside the bed.

5.4. Bubble identification and tracking

The presence of bubbles inherently introduces some inhomogeneity in the conditions experienced by the gas entering the reactor. This non-uniformity is apparent in the large variation of residence times, shown to be directly related to the local gas volume fraction (Fig. 13). Instantaneous velocity fields clearly show that the gas entering a bubble is channeled through it until it reaches the top of the bed, hence strongly reducing further mixing with the gas in the denser parts of the bed. As a first step toward a more fundamental understanding of the role of bubbles during fluidization, especially for reactive systems, a systematic way to identify and characterize bubbles has been devised and used to quantify the differences in bubbling behavior for various regimes.

5.4.1. Methodology

In this work, the method used by Herrmann [61] to identify liquid droplets in primary atomization simulations has been applied to bubble identification. A brief summary of the parallel version of the algorithm is given here, the reader being referred to Herrmann's work for more details. At each time step, the Eulerian gas volume fraction is computed from the location of the Lagrangian particles using the mollification approach described in Section 3.2. A grid cell is then assumed to be part of a bubble if its gas volume fraction is greater than a pre-defined threshold,

$$\varepsilon_f > \varepsilon_{f,\mathrm{cut-off}}. \tag{24}$$

The first step in the bubble identification algorithm is for each processor to assign a unique tag to each contiguous region satisfying Eq. 24. This is accomplished using a banded approach: when an untagged cell is found, it is assigned a tag, and this tag is propagated to surrounding cells if they match the cutoff criterion as well. A look-up table is then created to allow fast access to all grid cells belonging to a given structure. Since large bubbles are likely to span a region distributed over several processors, a synchronization step is required to assign the same tag to structures reaching across processors and periodic boundaries. Once each continuous structure is identified by a unique tag over the entire computation domain, several key quantities are computed by looping over the cells associated with this tag, including total volume defined as

$$V_{b,\mathrm{id}} = \sum_{\mathrm{tag}_i=\mathrm{id}} V_i, \tag{25}$$

center of gravity, written

$$x_{b,\mathrm{id}} = \frac{1}{V_{b,\mathrm{id}}} \sum_{\mathrm{tag}_i=\mathrm{id}} x_i V_i, \tag{26}$$

and moments of inertia as

$$I_{\mathrm{id}} = \begin{bmatrix} \sum_{\mathrm{tag}_i=\mathrm{id}} V_i\left(y_i^2+z_i^2\right) & -\sum_{\mathrm{tag}_i=\mathrm{id}} V_i x_i y_i & -\sum_{\mathrm{tag}_i=\mathrm{id}} V_i x_i z_i \\ -\sum_{\mathrm{tag}_i=\mathrm{id}} V_i x_i y_i & \sum_{\mathrm{tag}_i=\mathrm{id}} V_i\left(x_i^2+z_i^2\right) & -\sum_{\mathrm{tag}_i=\mathrm{id}} V_i y_i z_i \\ -\sum_{\mathrm{tag}_i=\mathrm{id}} V_i x_i z_i & -\sum_{\mathrm{tag}_i=\mathrm{id}} V_i y_i z_i & \sum_{\mathrm{tag}_i=\mathrm{id}} V_i\left(x_i^2+y_i^2\right) \end{bmatrix}. \tag{27}$$

V_i and x_i are the volume and Cartesian location of gas cell i, respectively. The bubble volume V_b is chosen to be the physical volume formed by all contiguous cells satisfying Eq. 24, ignoring the particles trapped inside the bubble. The principal axes and principal moments of inertia of each structure are obtained from an eigenvalue/eigenvector analysis and are used to construct an equivalent ellipsoid with the same moments of inertia, which radii are defined as

$$a_{\mathrm{id}} = \sqrt{\frac{5}{2}\frac{I_{1,\mathrm{id}} + I_{2,\mathrm{id}} + I_{3,\mathrm{id}}}{V_{\mathrm{id}}}}, \tag{28}$$

$$b_{\mathrm{id}} = \sqrt{\frac{5}{2}\frac{I_{1,\mathrm{id}} + I_{2,\mathrm{id}} + I_{3,\mathrm{id}}}{V_{\mathrm{id}}}}, \tag{29}$$

$$c_{\mathrm{id}} = \sqrt{\frac{5}{2}\frac{I_{1,\mathrm{id}} + I_{2,\mathrm{id}} + I_{3,\mathrm{id}}}{V_{\mathrm{id}}}}, \tag{30}$$

I_1, I_2, and I_3 being the principal moments of inertia of the bubble "id". An example of bubble identification and shape characterization is given in Fig. 14 in a two-dimensional case. $\varepsilon_{\mathrm{cut-off}}$ is set to 0.85 for all simulations presented in this work. While the exact value of this cut-off parameter is quite arbitrary, it was found to little affect bubble statistics thanks to sharp interfaces between bubbles and dense phase. Once a bubble becomes connected to the freeboard

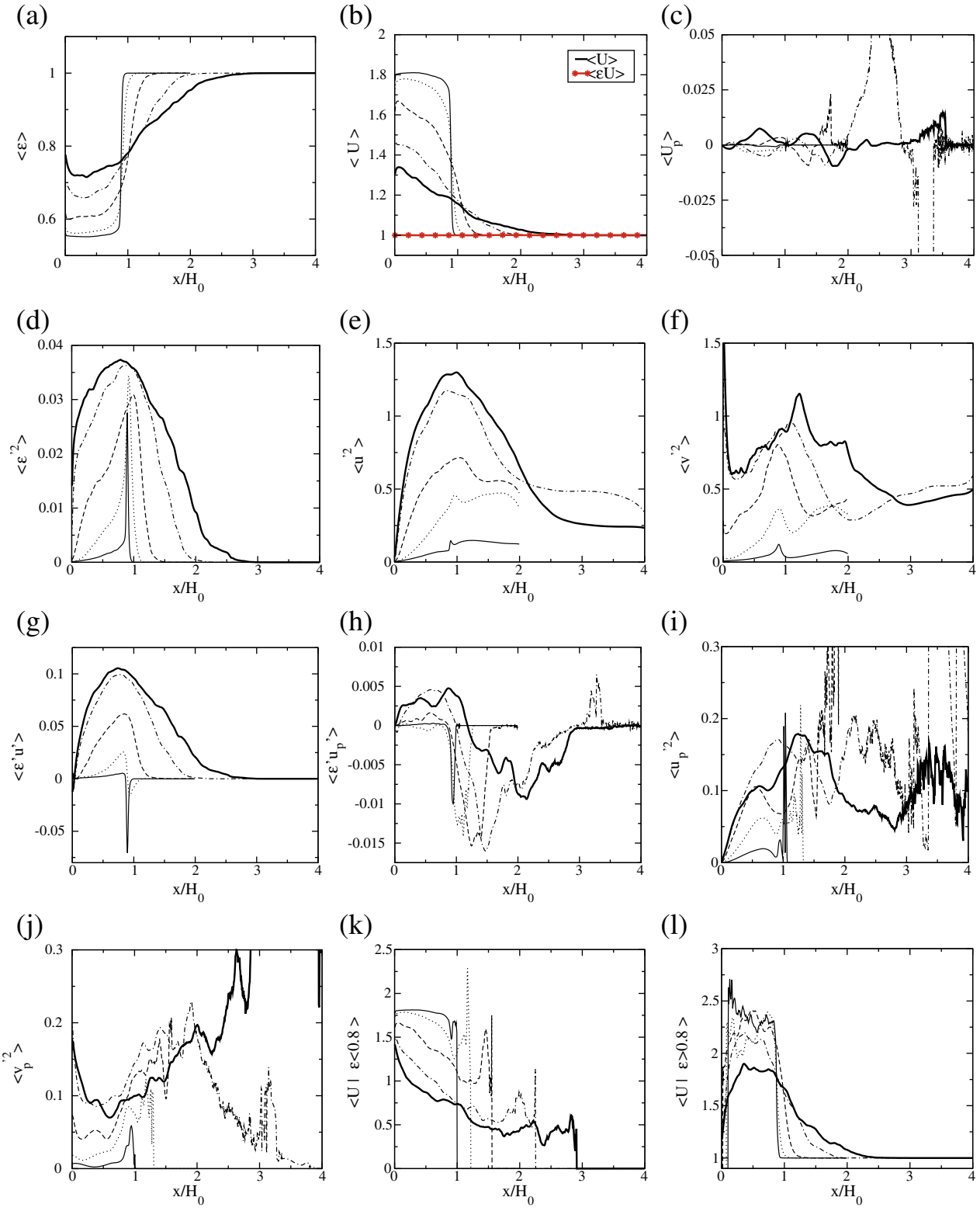

Fig. 8. Gas volume fraction and velocity statistics of 2D fluidized beds for different inlet velocities (*R1* to *R5*). From left to right, top to bottom: mean gas volume fraction ε_f, mean gas axial velocity, mean particle axial velocity, rms of ε_f, rms of axial and cross-streamwise gas velocity, correlation of ε_f and gas axial velocity fluctuations, correlation of ε_f and particle axial velocity fluctuations, rms of axial and cross-streamwise particle velocity, mean axial gas velocity conditioned on low and high values of ε_f. $U_{in} = 3.75\ U_{mf}$ (*R1*, thin solid line), $4\ U_{mf}$ (*R2*, dotted line), $5\ U_{mf}$ (*R3*, dashed line), $7\ U_{mf}$ (*R4*, dash-dotted line), and $9\ U_{mf}$ (*R5*, thick solid line).

region above the bed, it is removed from the list of bubbles. Particle positions and iso-contours of $\varepsilon_f = \varepsilon_{\text{cut-off}}$ are shown in Fig. 14(a) and (b). Fig. 14(c) shows the results of the identification algorithm: each bubble is depicted with two arrows aligned with the bubble principal axes, whose lengths are twice the radii of the equivalent ellipsoid. A disk with same area as the bubble is drawn at its center of gravity.

When bubble identification is carried out at a high enough frequency, it becomes possible to track each structure as it evolves through the bed. A bubble B_1 at time $t + \Delta t$ is assumed to be the

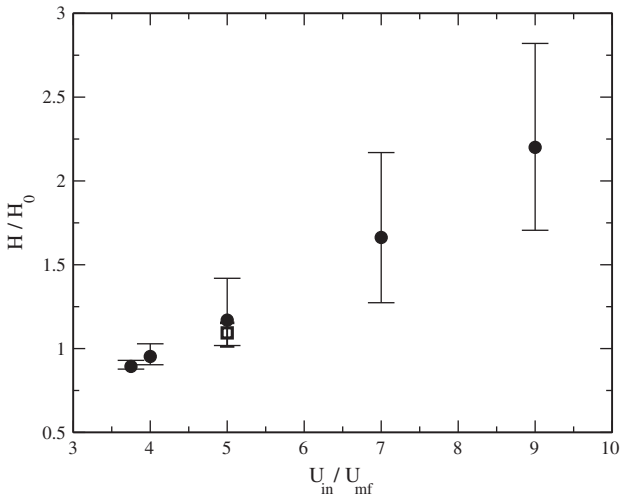

Fig. 9. Bed height as function of the gas inlet velocity: 2D cases *R1* to *R5* (filled circles) and 3D case (open square). Error bars indicate maximum and minimum bed height observed during the simulations.

same structure as a bubble B_0 at time t if, from all bubbles identified at time $t+\Delta t$, the center of gravity of B_1 is the closest from B_0's, and they are not separated by more than a distance d_{max} taken to be twice the gas phase velocity at B_0's location integrated over the time step. This rather crude approach proved to be satisfactory in all cases studied here, allowing to clearly follow the largest structures, from inception to merging with other bubbles or bursting at the bed surface. If additional accuracy is needed, tracking the volume of each bubble in addition to its center of gravity would help in lifting any ambiguity on bubbles merging, and splitting. Results from bubble tracking for the 3D case are shown in Fig. 15.

The very short, erratic trajectories of the smallest bubbles have been filtered out to retain only the major bubbling events. In the present case for which wall effects have been removed, it is interesting to note that bubbles are shown to rise to the top of the bed following a relatively straight trajectory with little lateral displacement.

Both bubble identification and bubble tracking have been used to collect quantitative informations on bubble dynamics for the two- and three-dimensional simulations, and results for bubble number, size, shape, and rise velocity, are presented below.

5.4.2. Bubble statistics

For comparison purposes, an equivalent diameter D_e is defined for each bubble as the diameter of the disk (in 2D) or sphere (in 3D) with an identical volume. Fig. 16 compares the average number and equivalent diameter of bubbles present simultaneously at any given time for different fluidization velocities. Error bars indicate a variation of plus and minus one standard deviation about the mean bubble diameter.

As the inlet velocity increases, both the number and mean diameter of bubbles present simultaneously in the bed increase, which is consistent with the bed expanding more at higher velocities. The average instantaneous number of bubbles reaches a plateau beyond 7 U_{mf}, while the average diameter and standard deviation keep increasing. Two contributions to this plateau can be put forward. Bubbles, especially at high inlet velocity, become increasingly difficult to identify at the top of the bed due to the increased probability of being connected to the free-board above. Then, more instances are found for which a very large bubble occupies most of the bed for the highest velocity cases. The average bubble diameter from the 3D simulation is also shown in Fig. 16, and is found to be very close from the corresponding 2D case *R3*.

Probability density functions of bubble size for the various cases are presented in Fig. 17.

Fig. 17(a) considers bubble equivalent diameter D_e for the 2D cases *R1* to *R5*. As the fluidization velocity increases, larger bubbles are created, with the largest bubbles at 9 U_{mf} having a diameter up to 3 times larger than those at 3.75 U_{mf}. As observed elsewhere [27], the probability density functions roughly follow a log-normal distribution, whose variance increases significantly at high inlet velocities. This may indicate an evolution in the merging dynamics. The bubble size distribution for the 3D case is shown in Fig. 17(b), superimposed on the corresponding 2D results from case *R3*. While the differences remain small, the largest bubbles in 3D are comparatively smaller than in 2D, and there are a larger number of bubbles around the $H_0/10$ scale.

To characterize bubble shapes, aspect ratios were computed for all 2D cases following Busciglio et al. [26] approach, who defined aspect ratio as the ratio between the bubble maximum horizontal extension and its maximum vertical extension. Results are shown in Fig. 18.

In agreement with direct visualization of the particle positions, horizontal elongated bubbles are found at low inlet velocity, while circular shapes are predominant at higher fluidization velocities. Aspect ratios at low velocity are higher than the experimentally reported ones [26], probably because of the lack of friction in the numerical model. The shift of aspect ratios toward more circular shapes when the inlet velocity increases, which has been observed experimentally but could not be reproduced by the Eulerian model of Busciglio et al. [27], is adequately recovered here.

Finally, bubbles created in the 3D case are classified based on their shape. Two different eccentricities are computed from the equivalent radii of the bubbles: the meridional eccentricity, which relates the longest to the shortest length

$$\mathrm{ecc}_m = \frac{\sqrt{a^2-c^2}}{a}, \tag{31}$$

and the equatorial eccentricity, which relates the longest to the second longest length

$$\mathrm{ecc}_e = \frac{\sqrt{a^2-b^2}}{a}. \tag{32}$$

Eqs. 31 and 32 assume $a>b>c$. By construction, both are between 0 and 1, and ecc_m is always larger than ecc_e. A scatter plot of 3D bubble eccentricities is shown in Fig. 19.

Most bubbles have a tubular shape that evolves into a prolate shape as the bubbles expand, consistent with the formation of mushroom-shaped structures.

Empirical work commonly relates bubble rise velocity U_B with the square root of the equivalent bubble diameter D_e [62–64],

$$U_B = 0.71 g^{1/2} D_e^{1/2}. \tag{33}$$

In Fig. 20(a), this correlation is plotted together with the bubble rise velocities obtained from the bubble trajectories using central differencing in the 2D cases *R1* to *R5*.

A small dependence on the inlet velocity is observed, with the bubble rise velocity for a given bubble diameter increasing when the fluidization velocity is increased. For all two-dimensional cases considered, the rise velocity is found to be smaller than the one estimated from Eq. 33, but remains roughly proportional to $\sqrt{D_e}$. Results obtained in 3D are compared with the equivalent 2D case *R3* and Eq. 33 in Fig. 20(b). While the empirical trend is followed very closely for medium size bubbles, a larger scatter and higher velocities are found for the largest bubbles. Agreement between numerical results and Eq. 33 however, remains fair. The observed discrepancy for high diameters can be explained by the fact that the largest bubbles, found near the top of the bed, are more likely to connect to the upper part of

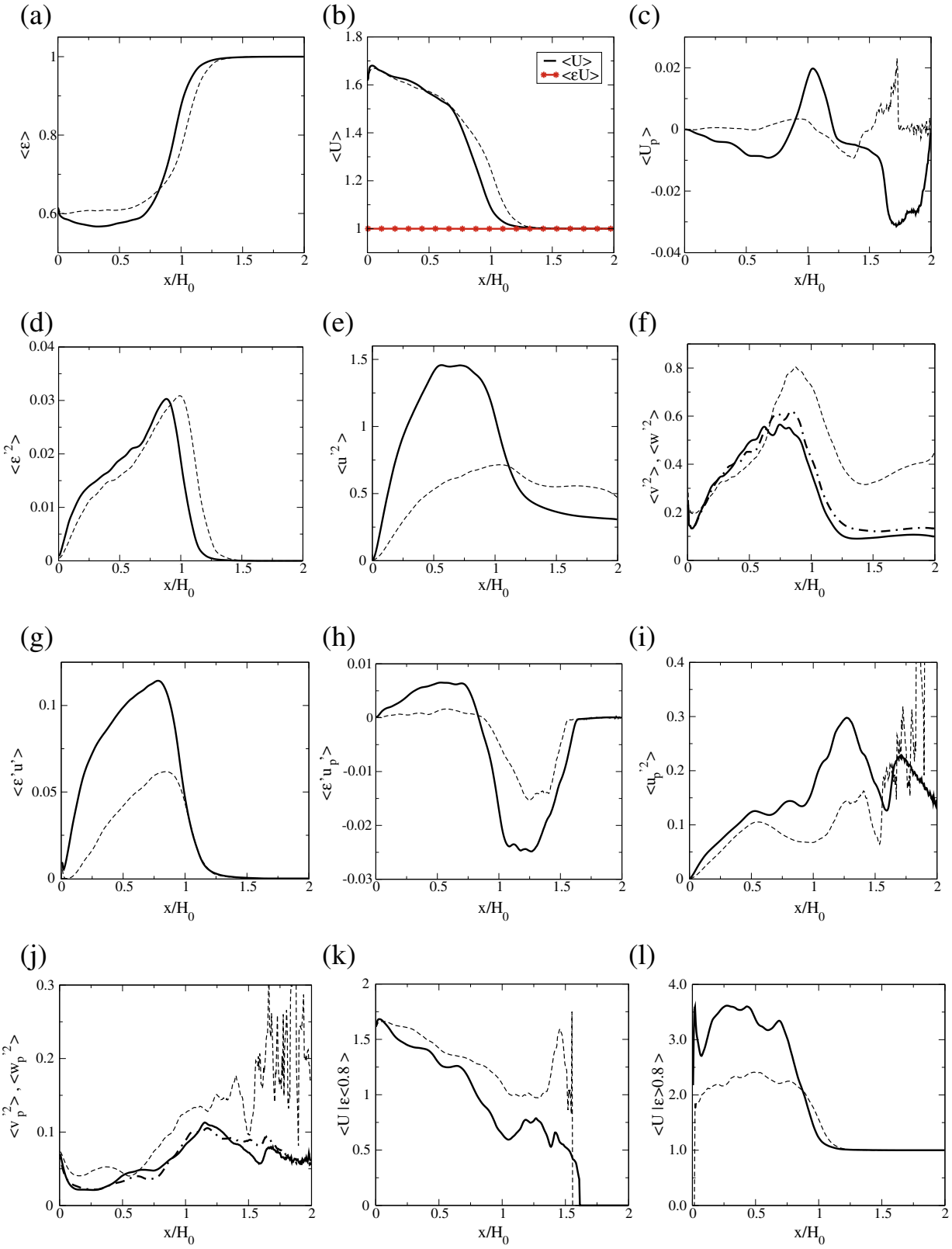

Fig. 10. Gas volume fraction and velocity statistics of 3D fluidized bed reactor (solid lines), compared with the equivalent 2D configuration *R3* (dashed lines). Variables shown are the same as in Fig. 8.

the reactor, and therefore, are not identified as individual bubbles anymore.

Correlations have been developed to estimate bubble diameter as a function of height in the reactor. One of the most successful correlations, used in numerous work [65–67], has been developed by Darton et al. [68], and relates the average bubble diameter to the gravity, the excess gas velocity and the height in the reactor, namely

$$D_b = 0.54\ \left(U_{in} - U_{mf}\right)^{0.4}\ \left(h + 4\sqrt{A_0}\right)^{0.8} g^{-0.2}. \tag{34}$$

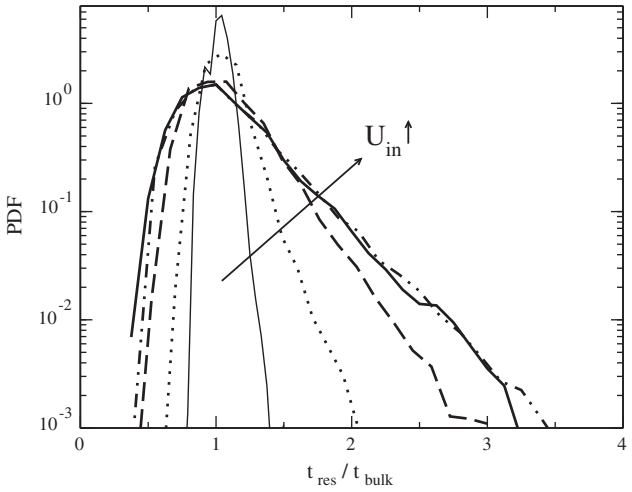

Fig. 11. PDF of normalized residence times in 2D fluidized beds: $U_{in} = 3.75\ U_{mf}$ (*R1*, thin solid line), $4\ U_{mf}$ (*R2*, dotted line), $5\ U_{mf}$ (*R3*, dashed line), $7\ U_{mf}$ (*R4*, dash-dotted line), and $9\ U_{mf}$ (*R5*, thick solid line).

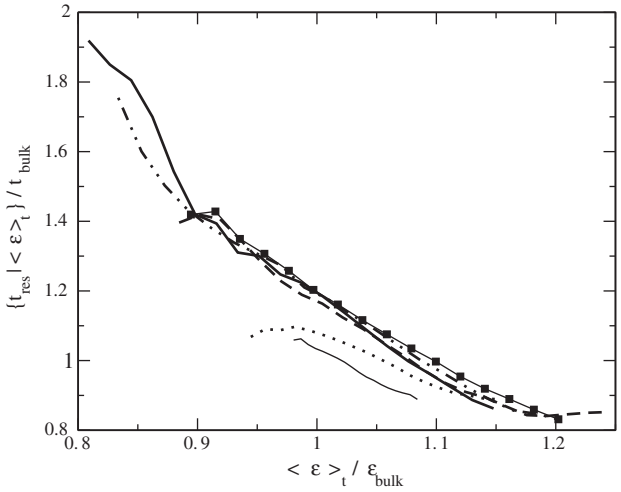

Fig. 13. Ensemble-averaged gas residence time inside the bed conditioned on the average gas volume fraction encountered on tracer trajectories. 2D cases: $U_{in} = 3.75\ U_{mf}$ (*R1*, thin solid line), $4\ U_{mf}$ (*R2*, dotted line), $5\ U_{mf}$ (*R3*, dashed line), $7\ U_{mf}$ (*R4*, dash-dotted line), and $9\ U_{mf}$ (*R5*, thick solid line), and 3D case (symbols).

In Eq. 34, A_0 is the catchment area of the distributor plate, i.e. the area of plate per orifice. Since in the simulations, a constant velocity is imposed over the entire inlet, a reasonable choice is to take A_0 to be equal to the grid cell area. This leads to $4\sqrt{A_0} = 1.56 \times 10^{-3}\ \mathrm{m}^2$. Simulation results for the number-averaged bubble diameter and Darton's correlation are shown in Fig. 21(a) for the two-dimensional cases, and a comparison between two- and three-dimensions at $U_{in} = 5\ U_{mf}$ is presented in Fig. 21(b).

The *x*-location of the bubbles is assumed to be the location of their center of gravity. In the two-dimensional cases, a good agreement was obtained between the numerical results and Darton's correlation for the highest inlet velocities considered, both for the magnitude of the diameter and the growth rate. While the growth rate is correctly reproduced at low fluidization velocities, the simulated bubbles are smaller than what is predicted by Darton et al. [68], possibly because of the absence of friction between particles. At $9\ U_{mf}$, the average diameter significantly decreases when reaching the top of the bed, which is again explained by the difficulty to correctly identify bubbles near the top of the bed. The number-averaged bubble diameter in the 3D case is slightly higher than in the corresponding 2D configuration, and thus, is in excellent agreement with the empirical correlation. The difference in mean diameter may be again explained in part by the difference in average gas volume fraction between two- and three-dimensional cases.

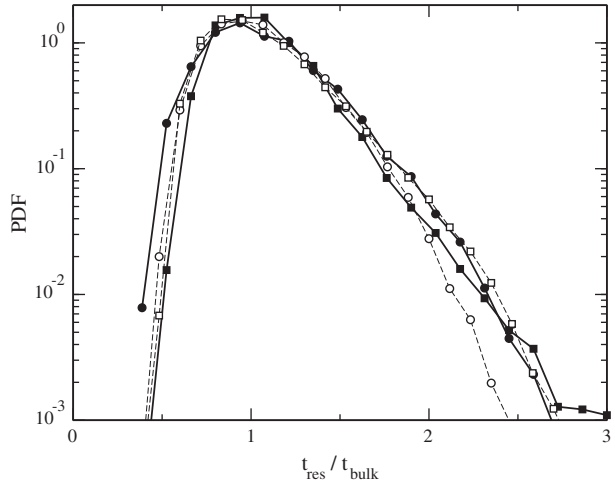

Fig. 12. PDF of normalized residence times inside the bed (filled symbols) and inside the reactor (open symbols): comparison between 2D (*R3* case, squares) and 3D (circles).

6. Conclusion

A numerical framework for the simulation of fluidized bed reactors using an Euler–Lagrange methodology has been developed and tested. A soft-sphere model is used to handle collisions, while a mollification algorithm is used to improve the accuracy of the gas–particle coupling for large particle diameter to mesh size ratios. The numerical approach followed provides good conservation properties and a very efficient parallelization, making it suitable for large-scale simulations involving $O(10^8)$ Lagrangian particles and Eulerian grid cells. Bubbling characteristics were also investigated using an efficient bubble identification and tracking strategy. Gas residence time distributions inside the bed have been obtained using tracer particles. Both 2D and 3D configurations have been investigated, each showing qualitatively expected behaviors. An analysis of the statistics for both 2D and 3D simulations has been carried out, the major findings being:

- Discrete particle methods are inherently three-dimensional since all gas–particle interaction models have been derived for spherical particles and therefore, are not directly applicable in 2D due to the different drag laws and packing characteristics of spheres and cylinders. This results in some arbitrariness in the definition of the gas volume fraction in 2D that may translate into significant differences in bed height and mean statistics for both ε_f and gas velocity;
- Noticeable differences in fluctuation statistics indicate that bed dynamics may not be entirely 2D and that inherently 3D dynamics may exist. This might explain the differences in bubble size and residence time distributions;
- Bubble size distributions roughly follow a log-normal law, the variances of which increase with inlet velocity. Excellent agreement was found for bubble rise velocity and bubble mean diameter inside the reactor between empirical correlations and numerical results for the 3D configuration. 2D results were able to predict the correct trends, but tended to under-predict both bubble velocity and diameter;

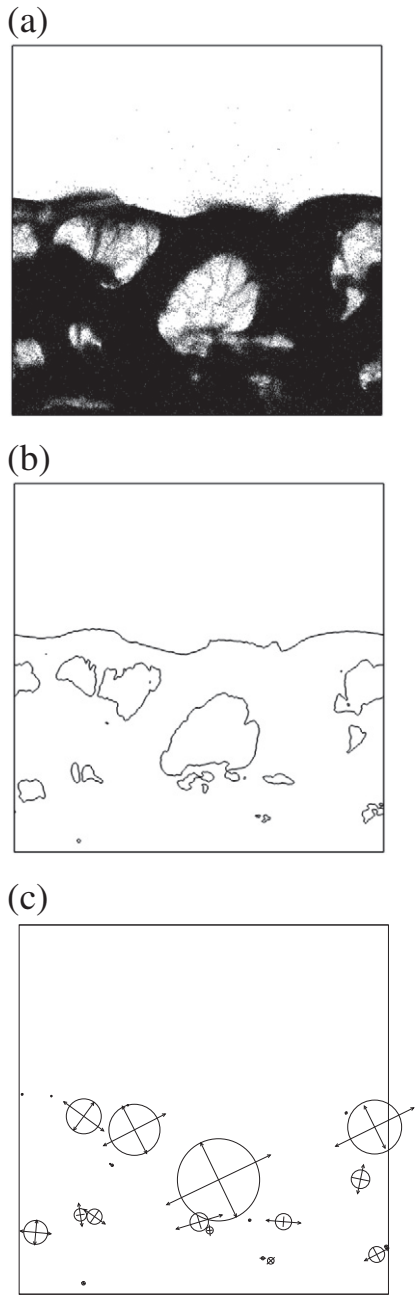

Fig. 14. Example of bubble identification from a snapshot of a two-dimensional fluidized bed simulation. (a) Particle positions. (b) Iso-contour of $\varepsilon_f = 0.85$. (c) Position, principal axes and equivalent area of identified bubbles.

- Bubble aspect ratios extracted from the 2D simulations reproduce experimentally observed trends that appeared to elude two-fluid models;
- The variance of the gas residence time distribution inside the bed increases significantly when the fluidization velocity increases. This is accompanied by an increased spread in porosity conditions encountered by the gas as it travels up the bed. Conditioning the residence time on the path-average gas volume fraction ε_t shows that residence time decreases linearly with the experienced porosity along the trajectory. This is similar for all cases investigated here, outlining a similar role of dense regions in trapping the gas inside the bed, and bubbles in propelling it upward.

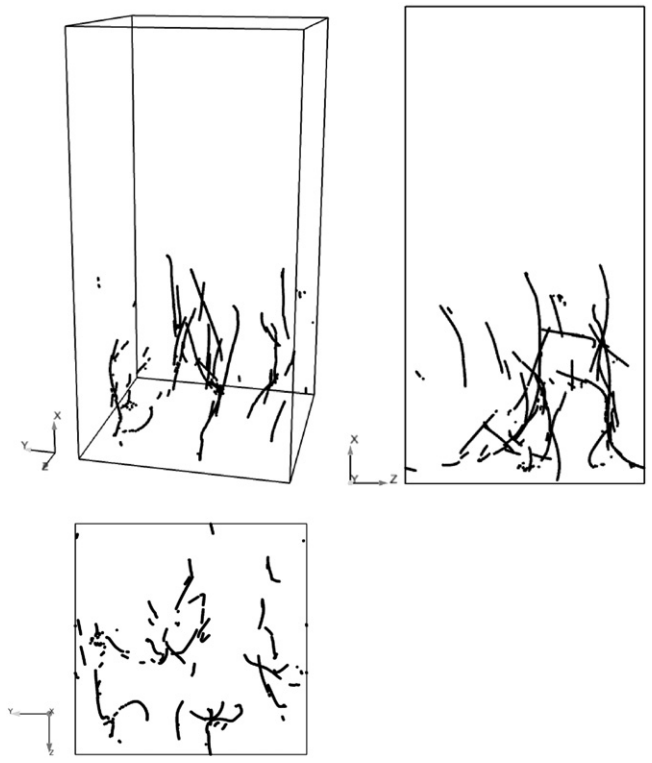

Fig. 15. Bubble trajectories observed in the 3D simulation: front perspective (top left), left side (top right), and top (bottom left) views.

With fluidization simulations done on up to 34 million particles and scalability studies on up to 382 million particles, this work highlights the potential for Lagrangian particle tracking approaches to simulate lab-scale systems such as the NREL 4 in. fluidized bed reactor, containing an estimated 200 million sand particles, with a one-to-one correspondence in terms of particle number. However, the present approach will be unable to handle larger, pilot or commercial scale systems without a modified treatment of the solid phase modeling. Those include Eulerian approaches, for which improved closure models can be developed from LPT simulations, or MP-PIC approaches in the context of large-eddy simulations.

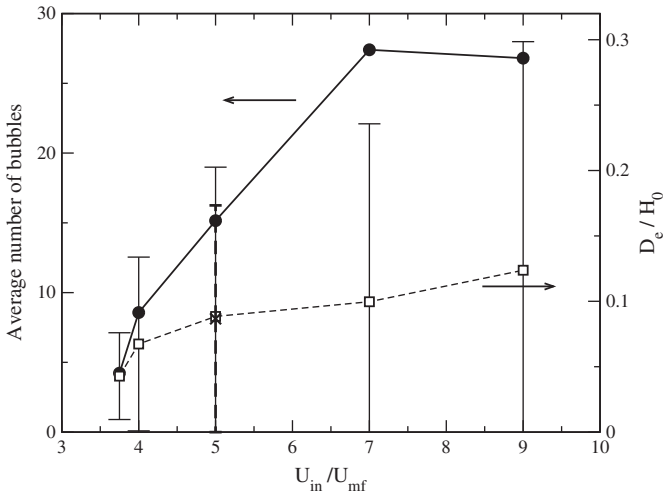

Fig. 16. Instantaneous average bubble number and equivalent diameter D_e in the bed for cases *R1* to *R5*. Cross and dashed error bar correspond to the 3D case.

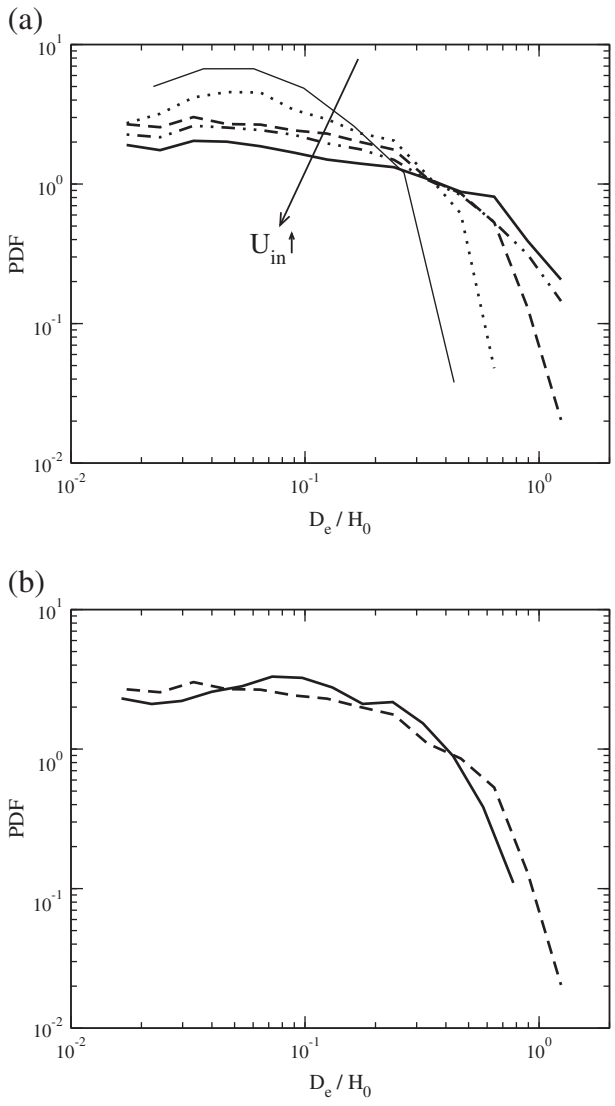

Fig. 17. Probability density function of bubble size during fluidization. (a) PDF of bubble equivalent diameter D_e for 2D cases. *R1* (3.75 U_{mf}, thin solid line), *R2* (4 U_{mf}, dotted line), *R3* (5 U_{mf}, dashed line), *R4* (7 U_{mf}, dash-dotted line), *R5* (9 U_{mf}, thick solid line). (b) Comparison of PDF of bubble equivalent diameter D_e between 3D (solid line) and 2D *R3* (dashed line) cases.

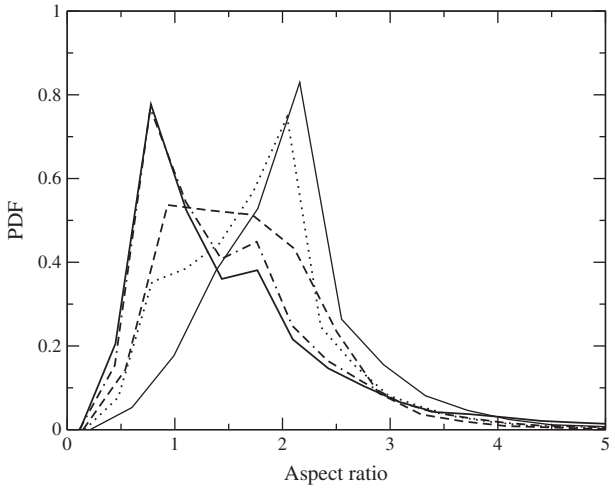

Fig. 18. Bubble aspect ratio distribution for different fluidization velocity: $U_{in} = 3.75\ U_{mf}$ (*R1*, thin solid line), 4 U_{mf} (*R2*, dotted line), 5 U_{mf} (*R3*, dashed line), 7 U_{mf} (*R4*, dash-dotted line), and 9 U_{mf} (*R5*, thick solid line).

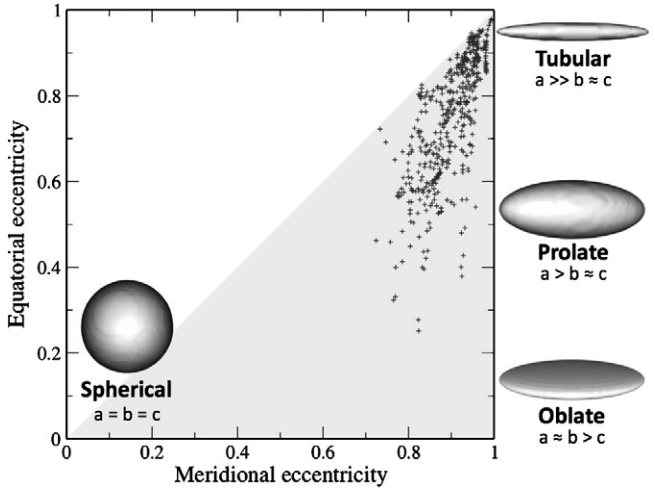

Fig. 19. Mapping between equatorial and meridional eccentricity of the bubbles identified in 3D case.

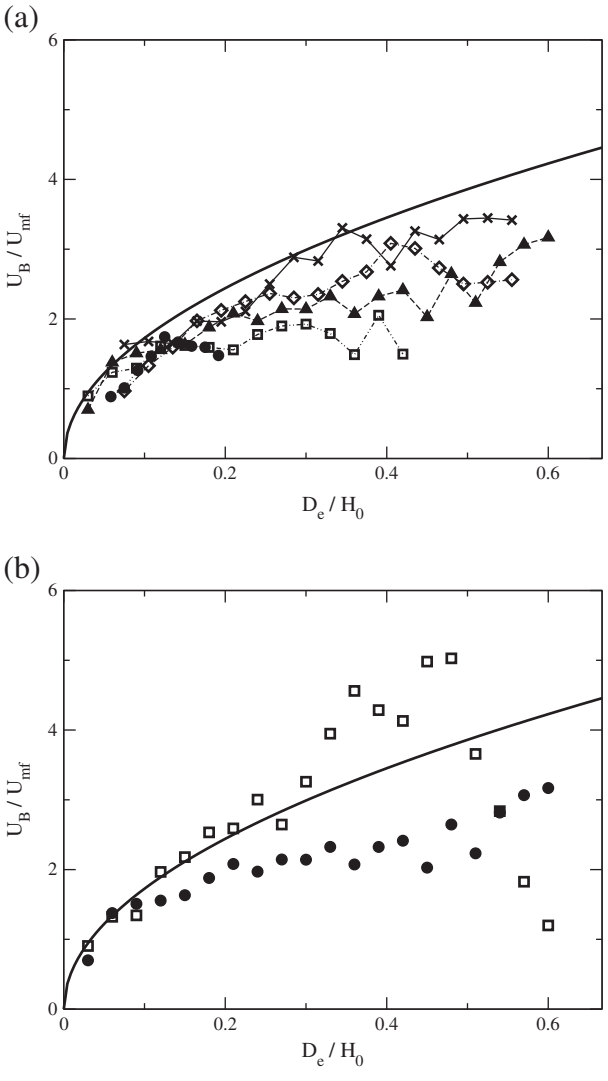

Fig. 20. 2D vs 3D: bubble rise velocity of the structures shown in Fig. 15: simulation (symbols) and experimental correlation for single bubbles (line, [62–64]). (a) Comparisons between Eq. 33 (solid line) and 2D numerical results (symbols): 3.75 U_{mf} (*R1*, filled circles), 4 U_{mf} (*R2*, open squares), 5 U_{mf} (*R3*, filled triangles), 7 U_{mf} (*R4*, open diamonds), and 9 U_{mf} (*R5*, cross). (b) Comparison between Eq. 33 (solid line), 2D (filled circles) and 3D (open squares) numerical results at 5 U_{mf}.

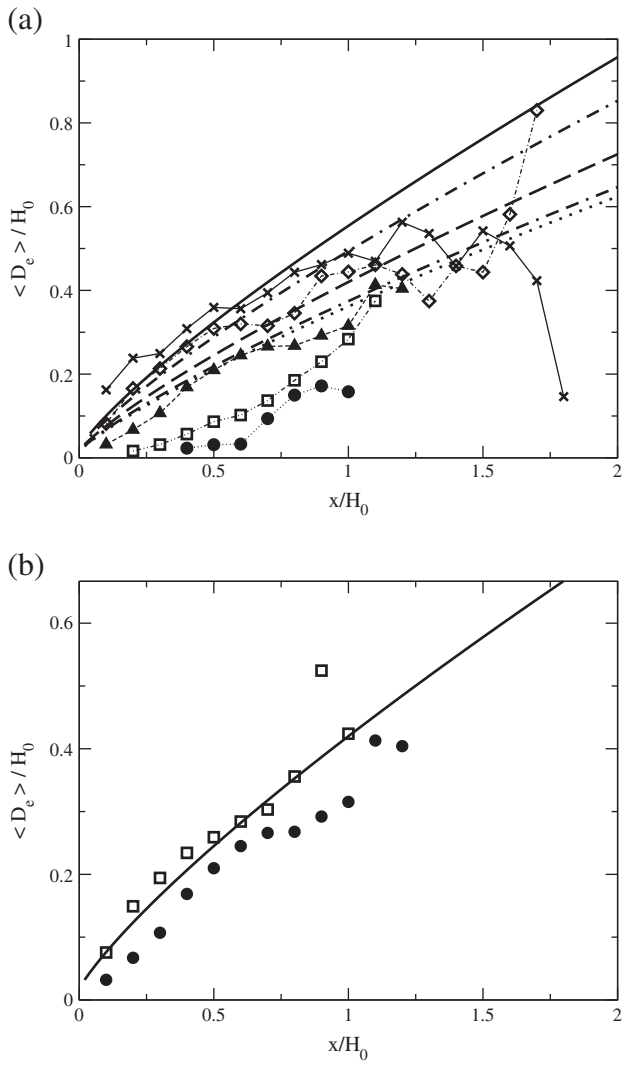

Fig. 21. Average bubble diameter: simulation (symbols) and experimental correlation from Darton et al. [68]. (a) Comparisons between Darton's correlation [a68] (lines) and 2D numerical results (symbols): 3.75 U_{mf} (filled circles, dotted line), 4 U_{mf} (open squares, double-dashed-dotted line), 5 U_{mf} (filled triangles, dashed line), 7 U_{mf} (open diamonds, dash-dotted line), and 9 U_{mf} (cross, solid line). (b) Comparison between Darton's correlation [68] (line), 2D (filled circles) and 3D (open squares) numerical results at 5 U_{mf}.

References

[1] S.D. Phillips, Technoeconomic analysis of a lignocellulosic biomass indirect gasification process to make ethanol via mixed alcohols synthesis, Industrial and Engineering Chemistry Research 46 (2007) 8887–8897.

[2] M.-K. Bahng, C. Mukarakate, D.J. Robichaud, M.R. Nimlos, Current technologies for analysis of biomass thermochemical processing: a review, Analytica Chimica Acta 651 (2009) 117–138.

[3] D. Gidaspow, Multiphase Flow and Fluidization: Continuum and Kinetic Theory Descriptions, Academic press, 1994.

[4] M. van Sint Annaland, G.A. Bokkers, M.J.V. Goldschmidt, O.O. Olaofe, M.A. van der Hoef, J.A.M. Kuipers, Development of a multi-fluid model for poly-disperse dense gas–solid fluidised beds, part I: model derivation and numerical implementation, Chemical Engineering Science 64 (2009) 4222–4236.

[5] O. Desjardins, R.O. Fox, P. Villedieu, A quadrature-based moment method for dilute fluid-particle flows, Journal of Comparative Physiology 227 (2008) 2514–2539.

[6] A. Passalacqua, R.O. Fox, R. Garg, S. Subramaniam, A fully coupled quadrature-based moment method for dilute to moderately dilute fluid-particle flows, Chemical Engineering Science 65 (7) (2010) 2267–2283.

[7] C. Campbell, C. Brennen, Computer simulation of granular shear flows, Journal of Fluid Mechanics 151 (1985) 167–188.

[8] B.P.B. Hoomans, J.A.M. Kuipers, W.J. Briels, W.P.M. Van Swaaij, Discrete particle simulation of bubble and slug formation in a two-dimensional gas-fluidised bed: a hard-sphere approach, Chemical Engineering Science 51 (1996) 99–118.

[9] P.A. Cundall, O.D.L. Strack, A discrete numerical model for granular assemblies, Geotechnique (1979) 47–65.

[10] Y. Tsuji, T. Kawaguchi, T. Tanaka, Discrete particle simulation of two-dimensional fluidized-bed, Powder Technology 77 (1993) 79–87.

[11] S. Harris, D.G. Crighton, Solitons, solitary waves and voidage disturbances in gas-fluidized beds, Journal of Fluid Mechanics 266 (1994) 243–276.

[12] D.M. Snider, P.J. O'Rourke, M.J. Andrews, Sediment flow in inclined vessels calculated using a multiphase particle-in-cell model for dense particle flows, International Journal of Multiphase Flow 24 (1998) 1359–1382.

[13] N.G. Deen, M. Van Sint Annaland, M.A. Van Der Hoef, J.A.M. Kuipers, Review of discrete particle modeling of fluidized beds, Chemical Engineering Science 62 (2007) 28–44.

[14] N.A. Patankar, D.D. Joseph, Modeling and numerical simulation of particulate flows by the Eulerian–Lagrangian approach, International Journal of Multiphase Flow 27 (10) (2001) 1659–1684.

[15] B.H. Xu, A.B. Yu, Numerical simulation of the gas–solid flow in a fluidized bed by combining discrete particle method with computational fluid dynamics, Chemical Engineering Science 52 (1997) 2785–2809.

[16] D. Gera, M. Gautam, Y. Tsuji, Computer simulation of bubbles in large-particle fluidized beds, Powder Technology 98 (1998) 38–47.

[17] N.G. Deen, M. van Sint Annaland, J.A.M. Kuipers, Detailed computational and experimental fluid dynamics of fluidized beds, Applications Mathematics and Modeling 30 (2006) 1459–1471.

[18] R. Beetstra, M.A. van der Hoef, J.A.M. Kuipers, Numerical study of segregation using a new drag force correlation for polydisperse systems derived from Lattice–Boltzmann simulations, Chemical Engineering Science 62 (2007) 246–255.

[19] M. van Sint Annaland, G.A. Bokkers, M.J.V. Goldschmidt, O.O. Olaofe, M.A. van der Hoef, J.A.M. Kuipers, Development of a multi-fluid model for poly-disperse dense gas–solid fluidised beds, part II: segregation in binary particle mixtures, Chemical Engineering Science 64 (2009) 4237–4246.

[20] M.J.V. Goldschmidt, J.A.M. Kuipers, R. Beetstra, Hydrodynamic modelling of dense gas-fluidised beds: comparison of the kinetic theory of granular flow with 3D hard-sphere discrete particle simulations, Chemical Engineering Science 57 (2002) 2059–2075.

[21] L. Huilin, W. Shuyan, Z. Yunhua, L. Yang, D. Gidaspow, J. Ding, Prediction of particle motion in a two-dimensional bubbling fluidized bed using discrete hard-sphere model, Chemical Engineering Science 60 (2005) 3217–3231.

[22] J.R. van Ommen, R.F. Mudde, Measuring the gas–solids distribution in fluidized beds — a review, International Journal of Chemical Reactor Engineering 6 (2008) Review 3.

[23] M. Goldschmidt, J. Link, S. Mellema, J. Kuipers, Digital image analysis measurements of bed expansion and segregation dynamics in dense gas-fluidised beds, Powder Technology (2003) 135–159.

[24] M.J.V. Goldschmidt, R. Beetstra, J.A.M. Kuipers, Hydrodynamic modelling of dense gas-fluidised beds: comparison and validation of 3D discrete particle and continuum models, Powder Technology 142 (2004) 23–47.

[25] B.P.B. Hoomans, J.A.M. Kuipers, M.A. Mohd Salleh, M. Stein, J.P.K. Seville, Experimental validation of granular dynamics simulations of gas-fluidised beds with homogenous in-flow conditions using positron emission particle tracking, Powder Technology 116 (2001) 166–177.

[26] A. Busciglio, G. Vella, G. Micale, L. Rizzuti, Analysis of the bubbling behaviour of 2D gas solid fluidized beds. Part I. Digital image analysis technique, Chemical Engineering Journal 140 (2008) 398–413.

[27] A. Busciglio, G. Vella, G. Micale, L. Rizzuti, Analysis of the bubbling behaviour of 2D gas solid fluidized beds. Part II. Comparison between experiments and numerical simulations via digital image analysis technique, Chemical Engineering Journal 148 (2009) 145–163.

[28] T. Kawaguchi, T. Yoshida, Y. Tsuji, MRI measurement of particle velocity in spouted bed, JSEM 7 (2007) 12–16.

[29] L. van der Lee, B. Chandrasekaran, I. Hulme, A. Kantzas, M.E.G. Worley, A.B. Calgary, A non-invasive hydrodynamic study of gas–solid fluidised bed of linear low density polyethylene, The Canadian Journal of Chemical Engineering 83 (2005) 119–126.

[30] J. Werther, J.F. Davidson, D.L. Keairns, Influence of the distributor design of bubble characteristics in large diameter gas fluidized beds, Fluidization, Cambridge University Press, U.K. and N.Y, 1978.

[31] T. Heindel, J. Gray, T. Jensen, An X-ray system for visualizing fluid flows, Flow Measurement and Instrumentation 19 (2008) 67–78.

[32] M. Deza, N.P. Franka, T.J. Heindel, F. Battaglia, CFD modeling and X-ray imaging of biomass in a fluidized bed, Journal of Fluids Engineering 131 (2009) 111303–1.

[33] N. Franka, T. Heindel, Local time-averaged gas holdup in a fluidized bed with side air injection using X-ray computed tomography, Powder Technology 193 (2009) 69–78.

[34] J. Min, J. Drake, T. Heindel, R.O. Fox, Experimental validation of CFD simulations of a lab-scale fluidized-bed reactor with and without side-gas injection, AICHE Journal 56 (2010) 1434–1446.

[35] E. Peirano, V. Delloume, B. Leckner, Two- or three-dimensional simulations of turbulent gas–solid flows applied to fluidization, Chemical Engineering Science 56 (2001) 4787–4799.

[36] N. Xie, F. Battaglia, S. Pannala, Effects of using two- versus three-dimensional computational modeling of fluidized beds — part I, hydrodynamics, Powder Technology 182 (2008) 1–13.

[37] N. Xie, F. Battaglia, S. Pannala, Effects of using two- versus three-dimensional computational modeling of fluidized beds: part II, budget analysis, Powder Technology 182 (2008) 14–24.

[38] T. Anderson, R. Jackson, Fluid mechanical description of fluidized beds. Equations of motion, Industrial and Engineering Chemistry 6 (1967) 527–529.

[39] D.Z. Zhang, A. Prosperetti, Momentum and energy equations for disperse two-phase flows and their closure for dilute suspensions, International Journal of Multiphase Flow 23 (1997) 425–453.
[40] A. Di Renzo, F.P. Di Maio, Homogeneous and bubbling fluidization regimes in DEM–CFD simulations: hydrodynamic stability of gas and liquid fluidized beds, Chemical Engineering Science 62 (2007) 116–130.
[41] K. Kafui, C. Thornton, M. Adams, Discrete particle-continuum fluid modelling of gas–solid fluidised beds, Chemical Engineering Science 57 (2002) 2395–2410.
[42] R. Beetstra, M.A. van der Hoef, J.A.M. Kuipers, Drag force of intermediate reynolds number flow past mono- and bidisperse arrays of spheres, AICHE Journal 53 (2) (2007) 489–501.
[43] O. Desjardins, G. Blanquart, G. Balarac, H. Pitsch, High order conservative finite difference scheme for variable density low Mach number turbulent flows, Journal of Comparative Physiology 227 (15) (2008) 7125–7159.
[44] O. Desjardins, V. Moureau, H. Pitsch, An accurate conservative level set/ghost fluid method for simulating primary atomization, Journal of Comparative Physiology 227 (18) (2008) 8395–8416.
[45] O. Desjardins, H. Pitsch, A spectrally refined interface approach for simulating multiphase flows, Journal of Comparative Physiology 228 (2009) 1658–1677.
[46] B.P. Van Poppel, O. Desjardins, J.W. Daily, A ghost fluid, level set methodology for simulating multiphase electrohydrodynamic flows with application to liquid fuel injection, Journal of Comparative Physiology 229 (2010) 7977–7996.
[47] O. Desjardins, H. Pitsch, Detailed numerical investigation of turbulent atomization of liquid jets, Atomization and Sprays 20 (2010) 311–336.
[48] O. Desjardins, H. Pitsch, Modeling effect of spray evaporation on turbulent combustion, 10th ICLASS, Kyoto, Japan, 2006.
[49] E. Knudsen, H. Pitsch, A dynamic model for the turbulent burning velocity for large eddy simulation of premixed combustion, Combustion and Flame 154 (2008) 740–760.
[50] E. Knudsen, H. Pitsch, A general flamelet transformation useful for distinguishing between premixed and non-premixed modes of combustion, Combustion and Flame 156 (2009) 678–696.
[51] L. Wang, H. Pitsch, Prediction of pollutant emissions from industrial furnaces using large eddy simulation, 5th US Combustion Meeting, San Diego, CA, 2007.
[52] C.D. Pierce, P. Moin, Progress-variable approach for large eddy simulation of turbulent combustion, Tech. Rep. TF80, Flow Physics and Computation Division, Dept. Mech. Eng, Stanford University, 2001.
[53] J. Kim, P. Moin, Application of a fractional-step method to incompressible Navier–Stokes equations, Journal of Computational Physics 59 (1985) 308–323.
[54] J.E. Dendy, Black-box multigrid for systems, Applications Mathematics and Computer 19 (1986) 57–74.
[55] O. Desjardins, P. Pepiot, Analysis of dense particulate flow dynamics using a Euler–Lagrange approach, Proceedings of 2010 Spring Meeting of the Western State Section of The Combustion Institute, Boulder, CO, 2010.
[56] K.R. Gaston, M.W. Jarvis, K.M. Smith, P. Pepiot, W.J. Frederick, M.R. Nimlos, Biomass pyrolysis and gasification of varying particle sizes in a fluidized bed reactor, Energy and Fuel (2010) accepted.
[57] Y.T. Makkawi, P.C. Wright, Fluidization regimes in a conventional fluidized bed characterized by means of electrical capacitance tomography, Chemical Engineering Science 57 (2002) 2411–2437.
[58] B.G.M. Van Wachem, J. Van der Schaaf, J.C. Schouten, R. Krishna, C.M. Van den Bleek, Experimental validation of Lagrangian–Eulerian simulations of fluidized beds, Powder Technology 116 (2001) 155–165.
[59] M.W. Jarvis, T.J. Haas, B.S. Donohoe, J.W. Daily, K.R. Gaston, W.J. Frederick, M.R. Nimlos, Elucidation of Biomass Pyrolysis Products Using a Laminar Entrained Flow Reactor and Char Particle Imaging, Energy Fuels 25 (1) (2011) 324–336, doi:10.1021/ef100832.
[60] P. Pepiot, M.W. Jarvis, M.R. Nimlos, G. Blanquart, Chemical kinetic modeling of tar formation during biomass gasification, Proceedings of 2010 Spring Meeting of the Western State Section of The Combustion Institute, Boulder, CO, 2010.
[61] M. Herrmann, A parallel Eulerian interface tracking/Lagrangian point particle multi-scale coupling procedure, Journal of Comparative Physiology 229 (2010) 745–759.
[62] S.A. Allahwala, O.E. Potter, Rise velocity equation for isolated bubbles and for isolated slugs in fluidized beds, Industrial and Engineering Chemistry Fundamentals 18 (1979) 112–116.
[63] W.H. Park, W.K. Kang, C.E. Capes, G.L. Osberg, The properties of bubbles in fluidized beds of conducting particles as measured by an electroresistivity probe, Chemical Engineering Science 24 (1969) 851–865.
[64] J.F. Davidson, D. Harrison, Fluidised Particles, Cambridge University Press, 1963.
[65] R. Clift, J.R. Grace, Fluidization, Academic Press, London, 1985.
[66] J.G. Yates, R.S. Ruiz-Martinez, D.J. Cheesman, Prediction of bubble size in a fluidized bed containing horizontal tubes, Chemical Engineering Science 45 (1990) 1105–1111.
[67] D.J. Patil, M. van Sint Annaland, J.A.M. Kuipers, Critical comparison of hydrodynamic models for gas–solid fluidized beds—part II: freely bubbling gas–solid fluidized beds, Chemical Engineering Science 60 (2005) 73–84.
[68] R.C. Darton, R.D. Lanauze, J.F. Davidson, D. Harrison, Bubble-growth due to coalescence in fluidized beds, Transactions of the Institute Chemical Engineering London 55 (1977) 274–280.